



An orientation corrected shaking method for the microstructure generation of short fiber-reinforced composites with almost planar fiber orientation

Celine Lauff^a, Matti Schneider^a, John Montesano^b, Thomas Böhlke^{a,*}

^a Karlsruhe Institute of Technology (KIT), Institute for Engineering Mechanics, Germany

^b University of Waterloo, Department of Mechanical and Mechatronics Engineering, Canada

ARTICLE INFO

Keywords:

Microstructure generation
Short fiber-reinforced composite
Representative volume element
Fiber orientation tensors
Fiber length distribution

ABSTRACT

We present an algorithm for generating short fiber-reinforced microstructures with almost planar fiber orientation. The orientation corrected shaking (OCS) method achieves a high accuracy regarding the volume fraction, fiber length distribution and fiber orientation state. Additionally, the algorithm is capable of generating microstructures for industrial materials, e.g., for a PA66GF35 material with a volume fraction of 19.3% and an aspect ratio of 33. For typical manufacturing processes, short fiber-reinforced composites show a mainly planar fiber arrangement. Therefore, we extend the two-step shaking algorithm of Li et al. [J. Ind. Text. 51(1), pp. 506–530, 2022] for a user-selected rectangular size of the unit cell and periodic boundary conditions. Additionally, the hidden closure structure of the algorithm is uncovered and a precise realization of the fiber orientation state achieved. We examine the representative volume element size for the OCS method, observing representative errors below 2% even for unit cells with edge lengths smaller than the mean fiber length. Additionally, the influence of different closure approximations on the stiffness is investigated. When applied to an industrial PA66GF35 material with sandwich structure, the OCS method demonstrates differences below 2% and 9% for the computed directional Young's moduli E_1 and E_2 compared to experimental data.

1. Introduction

1.1. State of the art

Discontinuous short fiber-reinforced polymers are used frequently in lightweight design due to their advantageous high specific stiffness and design freedom. As a result of the manufacturing process, the composites are highly anisotropic and the descriptive components, such as volume fraction, and fiber length and orientation distribution, vary throughout the component. To obtain the necessary three-dimensional information on the microstructure, micro-CT imaging is typically used [1,2]. Computational homogenization techniques [3] based on the theory of homogenization [4,5] are strategies capable of predicting the effective properties of heterogeneous materials complementing the oftentimes time-consuming experimental measurements.

For the respective full-field simulations on the microscale, synthetic, i.e., generated, microstructures complement data obtained from 3D imaging. Due to their random microstructure, discontinuous short fiber/reinforced polymers feature non/periodic geometries on the microscale. Several procedures for stochastic homogenization of non/periodic microstructures are available for classical [6–10] and micropolar continua [11,12]. Previous studies [6,7] revealed that when

considering periodic geometries in stochastic homogenization, utilizing periodic boundary conditions for the displacement fluctuation in mechanical problems leads to minimal artificial artifacts compared to other boundary conditions, e.g., displacement or traction boundary conditions. Obtaining periodic representative volume elements in stochastic homogenization is called periodization of random media, see Sab and Nadjar [13] for an introduction to the concept. Whereas periodizing microstructures obtained from tomographic data is non/trivial, microstructure generation offers the advantage that periodized samples are obtained quite naturally. Due to the negligible bending of short fibers, cylinder models describe such fibers accurately. Usually, the fiber orientation and the length distribution are considered independently, especially as data on coupling is available scarcely. Algorithms for generating microstructures of fiber-reinforced composites may be divided into two classes: sequential insertion algorithms and collective rearrangement algorithms.

In case of sequential insertion algorithms, the fibers are placed consecutively. Upon insertion of a fiber, both its direction and its midpoint are fixed. The most common algorithm in this class, the random sequential addition (RSA), is introduced by Widom [14] for spheres and

* Corresponding author.

E-mail address: thomas.boehlke@kit.edu (T. Böhlke).

<https://doi.org/10.1016/j.compstruct.2023.117352>

Received 6 March 2023; Received in revised form 8 May 2023; Accepted 10 July 2023

Available online 19 July 2023

0263-8223/© 2023 The Authors. Published by Elsevier Ltd. This is an open access article under the CC BY license (<http://creativecommons.org/licenses/by/4.0/>).

adapted for cylinders by Feder [15]. During the RSA algorithm, fibers are sampled randomly targeting a non-penetrating arrangement which moreover represents the descriptive statistics. However, the achievable volume fraction strongly decreases with increasing aspect ratio (the quotient of length and diameter) [16,17]. To overcome this limitation, several extensions of the RSA algorithm are proposed for short fiber-reinforced composites [18–21]. For the special case of discontinuous fiber-reinforced materials with non-uniformly dispersed and staggered aligned fibers, Bahmani et al. [22] present as extension the 3D staggered hard-core algorithm (SHCA). The method is capable of generating periodic geometries of aligned fibers for volume fractions up to 40% and accounting for different fiber aspect ratios in a computationally efficient way. Whereas a dense packing for aligned fiber orientation states is possible, even for high aspect ratios, still remains the question of how to generate synthetic microstructures for fiber reinforced composites with volume fractions and general fiber orientation states used in industry. Components made of fiber lengths exceeding the thickness, e.g., sheet molding compounds [23,24] and injection molding compounds [25,26], feature almost planar fiber arrangements. For these orientation states, Li et al. [27] present a two-step shaking algorithms, which is capable of achieving high density packings even for longer fibers. In an initial deterministic step, the fibers are first placed in a planar and non-penetrating setting. Subsequently, the fibers are shaken to introduce randomness and a deviation from planarity.

For collective rearrangement algorithms, all fibers change their midpoints and directions simultaneously until the target conditions, e.g., the non-penetration condition, are fulfilled. The mechanical contraction method (MCM) [28] of Williams and Philipse prepares a microstructure with non-overlapping particles and at a small volume fraction first, e.g., by the RSA method. Subsequently, the unit cell is contracted resulting in collisions between the fibers. To find a non-penetrating fiber arrangement, existing overlap is removed in an iterative way. In its original form, only isotropic fiber microstructures could be generated with MCM. For more general fiber orientation states, Schneider presents the sequential addition and migration (SAM) algorithm [29]. As a starting point, fiber midpoints and directions are sampled randomly according to the descriptive components of the microstructure. Due to the overlaps in the initial arrangement, subsequently a procedure similar to the mechanical contraction method is applied to remove the overlaps. In contrast to MCM, the overall fiber-orientation state is accounted for in the overlap removal. Hence, upon convergence the SAM algorithm produces microstructures where the non-penetration condition as well as the fiber orientation state is fulfilled. Based on the original algorithm, extensions of the SAM algorithm are given in Schneider [30] for long fibers with curvature and in Mehta and Schneider [31] for fiber length distributions.

1.2. Contributions

In this work, we introduce the Orientation Corrected Shaking (OCS) method based on the two-step shaking algorithm for almost planar fiber orientation states by Li et al. [27]. We address two main objectives for the generated microstructures. First, we aim to minimize the necessary representative volume element (RVE) size to reduce the time effort for the microstructure generation and computational homogenization. Secondly, we require an accurate realization of the fiber volume fraction, as well as the fiber length and orientation distributions.

For this purpose, we concern three restrictions of the algorithm provided by Li et al. [27]. First of all, the generated microstructures are fixed to an intrinsically calculated size of the rectangular unit cell. In particular only thin plate shapes are obtained. However, to investigate the representativity of different unit cell sizes, the size of the rectangular volume elements has to be chosen in an arbitrary way. Hence, we adapt the initial deterministic fiber placement to a modular procedure accounting for the user-selected dimensions of the unit cell.

The second restriction concerns the non-periodicity of the generated microstructures. In previous studies [6,7,13] it turns out that non-periodic geometries may adversely influence the representativity of a unit cell due to increased boundary condition artifacts. To reduce the necessary RVE size, we extend the algorithmic implementation, e.g., the inter-fiber overlap detection, to a periodic description of the geometry.

Last but not least, the fiber orientation state is not represented sufficiently by the original algorithm. Actually, the source of this restriction is twofold. First, Li et al. [27] control the fiber orientation state via fiber orientation tensors of second order. However, for computing the effective elastic properties accurately the fiber orientation tensor of fourth order is mandatory, see Müller and Böhlke [32]. The second cause concerns the shaking procedure of the fibers. Especially for increasing fiber alignment and volume fraction, deviations in the realized fiber orientation tensor of second order are obtained. To handle the latter two limitations, we provide an appropriate shaking strategy. More precisely, we uncover the hidden closure approximation of the shaking procedure. With this insight at hand, a semi-analytic estimation of the shaking parameters is identified and implemented. Moreover, we introduce the procedure of single orientation shaking to realize the fiber orientation tensor of fourth order accurately.

This article is organized as follows. Section 2 provides the terminology for short fiber-reinforced composites and details on the implementation of the fiber length distribution, as well as the inter-fiber overlap detection. In Section 3, we introduce the OCS method and describe the required extensions of the original two-step shaking algorithm [27]. Computational investigations on the implemented OCS method are conducted in Section 4. After studying the effect of the semi-analytic parameter estimation and the procedure of single orientation shaking, we discuss the necessary resolution and RVE size. Subsequently, the computed effective stiffness is compared to microstructures generated by the SAM algorithm based on the exact and the maximum entropy closure. Moreover, we apply the OCS method to an industrial PA66GF35 material and compare the results to experimental data, as well as to microstructures generated by the SAM algorithm. The appendix provides details for the semi-analytic estimation of the shaking parameters.

1.3. Notation

We represent vectors and tensors either in direct tensor notation or matrix representation with orthonormal basis $\{e_1, e_2, e_3\}$. Scalars are denoted by non-bold letters, e.g., b , vectors by bold lowercase letters, e.g., \mathbf{b} , tensors of second order by bold uppercase letters, e.g., \mathbf{B} , and tensors of fourth order by, e.g., \mathbb{B} . We represent tensors with varying tensor order by, e.g., $\mathbb{B}_{(l)}$, where l defines the tensor order. Second-order tensors parameterized with diagonal components read as, e.g., $\mathbf{B} \doteq \text{diag}(b_1, b_2, b_3)$. The transposition of a vector is written as, e.g., \mathbf{b}^\top . The scalar product is denoted by $\mathbf{A} \cdot \mathbf{B} = \text{tr}(\mathbf{A}\mathbf{B}^\top)$ and the Frobenius norm by $\|\mathbf{B}\| = (\mathbf{B} \cdot \mathbf{B})^{1/2}$. The linear mapping of a first-order by a second-order tensor reads as $\mathbf{a} = \mathbf{C}\mathbf{b}$ and the linear mapping with complete contraction including higher-order tensors as, e.g., $\mathbf{A} = \mathbb{C}[\mathbf{B}] \doteq C_{ijkl} B_{kl}$ using the summation convention. The dyadic product is symbolized by \otimes . The l -times repeated dyadic product of a vector is abbreviated, e.g., as $\mathbf{b}^{\otimes l} = \mathbf{b} \otimes \mathbf{b} \cdots \otimes \mathbf{b}$ (l repetitions). The unit sphere in \mathbb{R}^3 is denoted by S^2 .

2. Microstructure generation for short fiber-reinforced composites

2.1. Description of short fiber-reinforced composites

We consider a rectangular cell $Q = [0, Q_1] \times [0, Q_2] \times [0, Q_3]$ including N right circular cylindrical fibers in a non-penetrating fiber arrangement. The k th-fiber is characterized by the length L_k , the diameter D_k , the midpoint $\mathbf{x}_k \in Q$ and the direction $\mathbf{p}_k \in S^2$, see Fig. 1. We assume uniform fiber diameters $D = D_k$, but varying

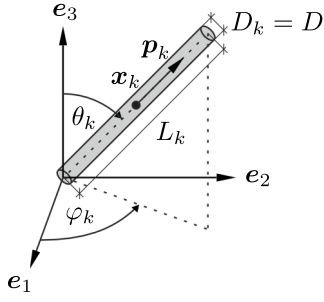


Fig. 1. Description of a short fiber.

fiber lengths following a given fiber length distribution $\rho(L_k)$. For short fiber-reinforced composites, the Weibull distribution [33] is often used [34–36]. Alternatively, the unit vector p_k may be represented by the angles θ_k and φ_k :

$$p_k \hat{=} \begin{bmatrix} \sin(\theta_k) \cos(\varphi_k) \\ \sin(\theta_k) \sin(\varphi_k) \\ \cos(\theta_k) \end{bmatrix}, \quad \theta_k, \varphi_k \in \mathbb{R}. \quad (2.1)$$

Notice that the angles θ_k and φ_k may be parameterized on the domain $[0, 2\pi)$ equivalently by accounting for the periodic characteristics of the trigonometrical functions throughout the article.

In a non-overlapping configuration, the fiber volume fraction ϕ computes as

$$\phi = \frac{\pi D^2}{4Q_1 Q_2 Q_3} L_{\text{total}} \quad (2.2)$$

with the total length

$$L_{\text{total}} = \sum_{k=1}^N L_k. \quad (2.3)$$

In this work, fiber orientation tensors are used as a compact characteristic of the fiber orientation distribution, see Advani et al. [37] and Kanatani [38]. Due to the finite number of fibers in a generated microstructure and the varying fiber lengths, the volume-weighted fiber orientation tensors of order l compute as

$$\mathbb{A}_{(l)} = \frac{1}{L_{\text{total}}} \sum_{k=1}^N L_k p_k^{\otimes l}. \quad (2.4)$$

For fiber-reinforced composites, micro-computed tomography is a convenient tool to estimate the fiber orientation tensors [39–41]. By applying mean field homogenization methods [25,32,42], it turns out that the effective properties can be approximated by functions of the first two moment tensors. For this reason, typically the second- and fourth-order tensors \mathbf{A} and \mathbb{A} are considered.

2.2. Prescribing the fiber length distribution

In this work, we use the Weibull distribution to describe the fiber lengths within the generated microstructures. It is defined via the density function [43, eq. (4-43)]

$$\rho_{\lambda,\beta}(L) = \frac{\beta}{\lambda} \left(\frac{L}{\lambda}\right)^{\beta-1} e^{-(L/\lambda)^\beta}, \quad L, \lambda, \beta > 0, \quad (2.5)$$

with the scale parameter λ and the shape parameter β . According to Mehta and Schneider [31] the Weibull parameters λ and β may be computed from given values for the volume-weighted mean m and standard deviation s . With this notation at hand, we assume the length L_k of the k th-fiber to follow the corresponding Weibull distribution, i.e.,

$$L_k \sim \text{Weibull}(m, s). \quad (2.6)$$

When generating microstructures, it is necessary to *sample* the fiber lengths with a specific sampling scheme. As result of the finite number of fibers, the selected sampling scheme may lead to an inaccurate fiber length distribution, e.g., characterized by a large deviation of the realized statistical moments compared to the moments of the distribution. Mehta and Schneider [31] study the introduced error of sampling with the classical Monte Carlo approach [44] and with scrambled or non-scrambled Sobol sequences [45,46]. Due to the smallest error for scrambled Sobol sequences, we use this scheme for the following investigations.

We terminate the sampling of fiber lengths whenever the prescribed volume fraction ϕ is exceeded. To match the targeted fiber volume fraction exactly, we rescale each fiber length individually with

$$L_k \leftarrow L_k \frac{4Q_1 Q_2 Q_3 \phi}{\pi D^2 L_{\text{total}}}. \quad (2.7)$$

2.3. Inter-fiber collision checks for periodic boundary conditions

To realize a non-penetrating fiber arrangement, it is necessary to compute the inter-fiber distances repeatedly, leading to a significant influence on the computational effort. To decrease the runtime, during the computation of the inter-fiber distances we model each fiber as a spherocylinder [28], i.e., a half sphere is attached to each end of the cylinder. Two spherocylinders intersect precisely if the smallest distance between the center lines of the fibers is smaller than the diameter D . For the numerical computation of the effective elastic properties with voxel-based grids, usually a minimum distance d_{\min} between the fibers is enforced to avoid excessively high stresses when fibers are too close [47,48]. To realize the minimum distance, the diameter of the fibers is increased only for the collision detection

$$D \leftarrow D + d_{\min}. \quad (2.8)$$

Notice that a minimum distance between the fibers leads to an increased runtime due to the artificially higher volume fraction during the collision checks. For instance, the volume fraction increases by 44% for a minimum distance of 20% of the fiber diameter.

For computing the smallest distance between the center lines of two fibers, we rely on the modification of the Vega-Lago algorithm [49] introduced by Pournin et al. [50]. For an efficient implementation of periodic boundary conditions, we use the minimum image convention strategy, commonly employed in molecular dynamics simulations, see, e.g., Deiters [51]. More precisely, for two particles only the distance between their closest periodic realizations is computed. For cylindrical fibers, an adaption of the scheme is presented, e.g., by Schneider [30], in case the fiber lengths are shorter than half of the smallest edge length. Considering the k th- and the j th-fiber, the three components ($i = 1, 2, 3$) of one of the fibers' midpoints are corrected only for the collision detection with

$$x_k^i \leftarrow \begin{cases} x_k^i - Q_i, & \text{if } x_k^i - x_j^i > Q_i/2 \\ x_k^i + Q_i, & \text{if } x_k^i - x_j^i < -Q_i/2 \\ x_k^i, & \text{else} \end{cases} \quad (2.9)$$

provided $L_j, L_k < \min(Q_1, Q_2, Q_3)/2$.

In case of a fiber length distribution with a high variance for strongly anisotropic cells, condition (2.9) may not be satisfied, as the fibers are too long. A simple workaround to treat longer fibers, introduced by Mehta and Schneider [31], proceeds by a divide and conquer strategy with respect to the fiber length.

Moreover, whenever a fiber exceeds a complete edge length, it is necessary to check self-intersection to ensure a non-overlapping configuration. We use the self-intersection scheme provided by Mehta and Schneider [31], which is activated for the k th-fiber if the condition

$$L_k p_k^i > Q_i - D \quad \text{with } i = 1, 2, 3 \quad (2.10)$$

is fulfilled for at least one of the three components.

3. The orientation corrected shaking method

3.1. The initial step

We assume the second-order fiber orientation tensor \mathbf{A} to be given in diagonal and ordered form

$$\mathbf{A} \hat{=} \text{diag}(a_1, a_2, a_3) \quad \text{with} \quad a_1 \geq a_2 \geq a_3. \quad (3.1)$$

A symmetric second order fiber orientation tensor may be brought into the form of Eq. (3.1) by an eigendecomposition and a rotation into the eigenbasis.

The two-step shaking method [27] assumes the third eigenvalue a_3 to be small. Therefore, an initial fiber orientation tensor $\tilde{\mathbf{A}}$ is introduced which attains the form

$$\tilde{\mathbf{A}} \hat{=} \text{diag}(\tilde{a}_1, \tilde{a}_2, 0) \quad \text{with} \quad \tilde{a}_i = \frac{a_i}{a_1 + a_2}, \quad i = 1, 2. \quad (3.2)$$

The presence of non-zero third component a_3 in the original fiber orientation tensor \mathbf{A} (3.1) will be accounted for in the shaking step.

In the initial step, the initial fiber orientation tensor $\tilde{\mathbf{a}}_1$ is realized by a deterministic arrangement of the fibers. According to Li et al. [27], the microstructure is divided into sublayers with aligned fibers. If the condition $\tilde{a}_1 < 0.6$ holds, a division into two sublayers will be used, where the standard unit vectors e_1 and e_2 represent the fiber directions of the sublayers. Alternatively, the directions are represented with the angles

$$\tilde{\theta}_1 = \frac{\pi}{2}, \tilde{\varphi}_1 = 0 \quad \text{and} \quad \tilde{\theta}_2 = \frac{\pi}{2}, \tilde{\varphi}_2 = \frac{\pi}{2}. \quad (3.3)$$

To fulfill the initial fiber orientation tensor $\tilde{\mathbf{A}}$, the sublayers with fibers in e_1 - or e_2 -direction are filled with fibers up to a volume fraction

$$\tilde{\phi}_1 = 2\tilde{a}_1\phi \quad \text{or} \quad \tilde{\phi}_2 = 2(1 - \tilde{a}_1)\phi. \quad (3.4)$$

For stronger alignment, i.e., under the condition $\tilde{a}_1 \geq 0.6$, the unit cell is divided into three sublayers to reduce the difference of the volume-fraction between the sublayers. Therefore, the fibers are placed in two sublayers with direction e_1 and in one sublayer with direction e_2 . The fiber volume fractions of the sublayers compute as

$$\tilde{\phi}_1 = 1.5\tilde{a}_1\phi, \quad \tilde{\phi}_2 = 3(1 - \tilde{a}_1)\phi. \quad (3.5)$$

In the algorithm introduced by Li et al. [27], the size of the initial filling space depends on the mean length of the fibers $L_{\text{mean}} = L_{\text{total}}/N$, the first eigenvalue of the fiber orientation tensor in the initial arrangement \tilde{a}_1 , the fiber volume fraction ϕ and the diameter of the fibers D . Furthermore, hard boundary conditions are considered leading to a low fiber content close to the boundaries. To overcome this problem, Li et al. choose larger dimensions $Q_{1,2}$ for the initial space than for the shaking step. Computational evidence suggests [6,7,13] that using periodic microstructures and periodic boundary conditions for computational homogenization minimizes boundary condition artifacts. For this reason, we consider an extension of the original algorithm to generate periodic unit cells. Additionally, as fibers can pass the boundaries without restriction, we use the same cell dimensions for the initial step and for the shaking step.

A second extension concerns the use of more than two or three sublayers, respectively. Indeed, we consider a repetition of the construction, compare Eqs. (3.4) and (3.5). In this way, we may investigate representativity of the structures in direction e_3 , as well. Therefore, the structure of $n_{\text{sub}} = 2$ (or $n_{\text{sub}} = 3$) layers is repeated n -times until the prescribed height is achieved. The height of the single sublayers h_{sub} is calculated with

$$c = \sqrt{\frac{\pi D^2}{2\tilde{\phi}_1}}, \quad n = \left\lfloor \max\left(\frac{Q_3}{n_{\text{sub}}c}, 1\right) \right\rfloor \quad \text{and} \quad h_{\text{sub}} = \frac{Q_3}{n_{\text{sub}}n}, \quad (3.6)$$

where the bracket type $\lfloor \cdot \rfloor$ denotes the floor function.

According to Li et al. [27], we decompose each sublayer into a row of smaller cells. In Fig. 2, schematically a single sublayer with

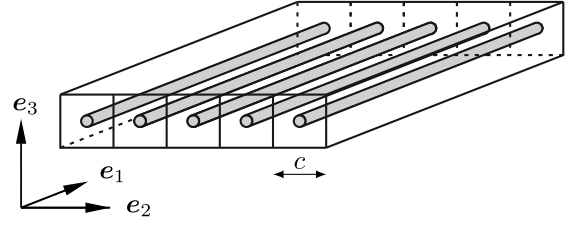


Fig. 2. Sublayer with a single continuous fiber per cell, compare Li et al. [27, Fig. 4(a)].

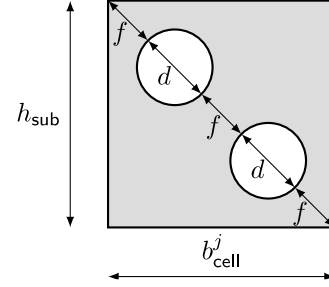


Fig. 3. Cross-section of a cell with two fibers.

continuous fibers in direction e_1 is shown consisting of five cells. The parameter c in Eq. (3.6) refers to the quadratic edge length of the cells and is computed under the assumption of continuous, i.e., infinitely long, fibers. For increasing the possible density of the initial packing, two fibers per cell are assumed (Z. Li, personal communication, January 17, 2022), see Fig. 3. Therefore, an additional factor $\sqrt{2}$ in Eq. (3.6) for the parameter c arises.

To fill the j th-sublayer, fiber lengths are sampled according to the fiber length distribution in a successive fashion and assigned to the first cell. If a fiber cannot be arranged without fiber intersection, a new cell will be filled. This procedure is terminated provided the target volume fraction is reached. In case its length exceeds the edge lengths, a fiber is exclusively assigned to a cell and fiber self-intersection in the initial step is accepted. We denote the number of cells considered in the j th-sublayer with n_{cell}^j .

The width of the cells b_{cell}^j , see Fig. 3, computes for each sublayer ($j = 1, \dots, n_{\text{sub}}n$) as

$$b_{\text{cell}}^j = \frac{b_{\text{sub}}^j}{n_{\text{cell}}^j}, \quad (3.7)$$

accounting for the number of cells n_{cell}^j considered in the sublayer and its total width b_{sub}^j – either Q_1 or Q_2 . As a consequence of the extension of the initial step proposed in the article at hand, the dimensions of a rectangular unit cell may be chosen in an arbitrary way. This contrasts with Li et al. [27], where the size of the unit cell is fixed.

In Fig. 4(a), an initial microstructure with edge length $Q_i = 500 \mu\text{m}$, lengths distributed according to $L_k \sim \text{Weibull}(m = 200 \mu\text{m}, s = 80 \mu\text{m})$, volume fraction $\phi = 20\%$, uniform diameter $D = 10 \mu\text{m}$ and second-order fiber orientation tensor $\mathbf{A} \hat{=} \text{diag}(0.49, 0.49, 0.02)$ is shown.

3.2. The shaking step

After the initial placement the fibers are shaken to introduce randomness. Li et al. [27] present a procedure where the fibers are shaken consecutively, using the initial arrangement as starting point. For every fiber, first intense shaking (*global shaking*) is applied. To ensure non-interpenetration of the fibers, a shaken fiber will be accepted if there is no collision with any fiber that has already been accepted. If within a maximum number of attempts m_{max} no admissible setting was found,

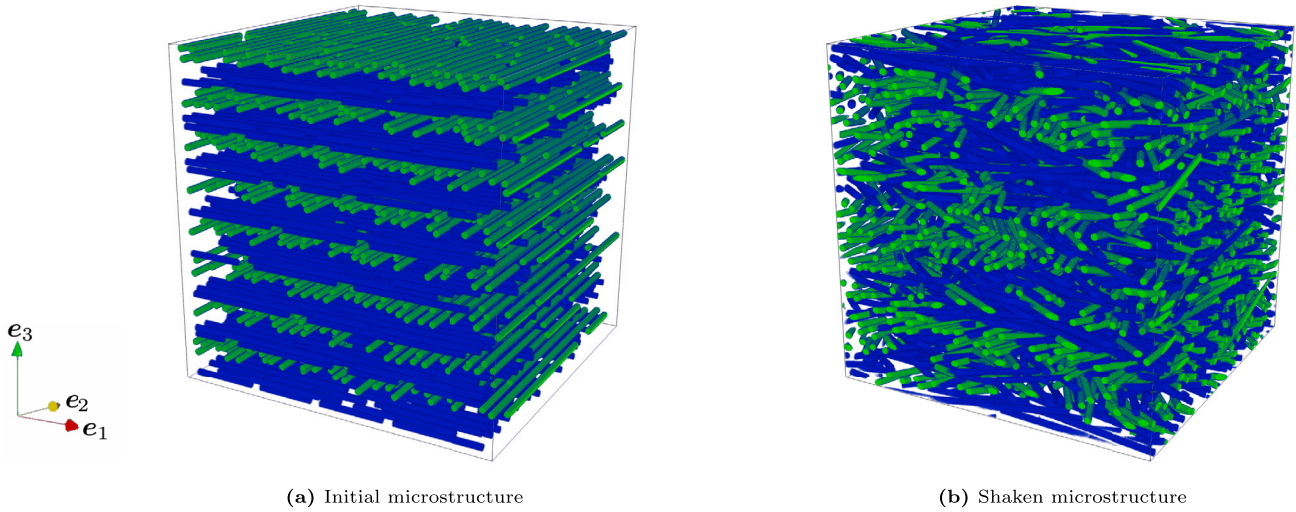


Fig. 4. Initial and shaken microstructure with edge length $Q_i = 500 \mu\text{m}$, volume fraction $\phi = 20\%$, lengths distributed according to $L_k \sim \text{Weibull}(m = 200 \mu\text{m}, s = 80 \mu\text{m})$, uniform diameter $D = 10 \mu\text{m}$ and second-order fiber orientation tensor $\mathbf{A} \hat{=} \text{diag}(0.49, 0.49, 0.02)$.

smaller shaking steps will be applied (*local shaking*). In case the fiber placement fails again, it will be broken into two smaller parts and they are shaken individually (*breaking and shaking*). Fibers which cannot be updated in one of these three steps are deleted. Broken or deleted fibers lead to errors in the fiber length distribution ρ and the fiber orientation tensor \mathbf{A} . The shaking procedure of the entire microstructure is repeated N_{max} -times. With increasing N_{max} , the intensity of shaking in a single iteration decreases [27, Eq. (14)].

In contrast to Li et al. [27], we only shake the entire microstructure once ($N_{\text{max}} = 1$) and use the procedure of *global shaking*, as this turns out to be sufficient for obtaining good results. Furthermore, we require that all fibers can be updated successfully to preserve the fiber length distribution ρ and the fiber orientation tensor \mathbf{A} .

Let us focus on the update of the midpoint and the direction of a single fiber during the shaking step. For every attempt $1 \leq m \leq m_{\text{max}}$, the midpoint of the k th-fiber is computed by adding a shaking step to the midpoint of the previous attempt:

$$\mathbf{x}_k^m \leftarrow \mathbf{x}_k^{m-1} + \Delta \mathbf{x}, \quad \Delta \mathbf{x} \hat{=} c [\alpha \xi_1 \quad \alpha \xi_2 \quad \beta \xi_3]^\top. \quad (3.8)$$

Randomness is introduced by the realizations ξ_1 , ξ_2 and ξ_3 of the normal distribution $\mathcal{N}(\mu = 0, \sigma^2 = 1/3)$ with mean $\mu = 0$ and variance $\sigma^2 = 1/3$. The parameter c follows Eq. (3.6). To control the intensity of the shaking, the parameters α and β are selected by trial and error. The location of the midpoint in the initial arrangement $\tilde{\mathbf{x}}_k$ is used as starting point for computing the midpoint of the first attempt.

The angles of the fibers with initial direction \mathbf{e}_i ($i = 1, 2$) are computed according to the sampling procedure

$$\theta_i \leftarrow \tilde{\theta}_i + \Delta\theta \xi_\theta = \frac{\pi}{2} + \Delta\theta \xi_\theta \quad \text{and} \quad \varphi_i \leftarrow \tilde{\varphi}_i + \Delta\varphi \xi_\varphi. \quad (3.9)$$

Notice that Eq. (3.9) depends on the initial direction \mathbf{e}_i but not on the specific fiber k or number of attempt m . The parameters $\Delta\theta$ and $\Delta\varphi$ control the intensity of the directional shaking and are set to

$$\Delta\theta = \gamma_1 \arcsin\left(\frac{Q_3}{L_f}\right) \quad \text{and} \quad \Delta\varphi = \gamma_2 \frac{\pi}{4}. \quad (3.10)$$

Similar to α and β , the shaking parameters γ_1 and γ_2 are selected by trial and error. Randomness is introduced by realizations ξ_θ and ξ_φ of the normal distribution $\mathcal{N}(0, 1/3)$. A pseudo-code for the OCS method is provided in Alg. 1 and a result of the shaking step visualized in Fig. 4(b).

Algorithm 1: OCS method with multiple orientation shaking

- 1: **Initial Step**
 - 2: Arrange fibers in orthogonal layers according to ϕ , $\rho_{\lambda,\beta}(L_k)$, $\tilde{\mathbf{A}}$ and \mathcal{Q}
 - 3: **Shaking Step**
 - 4: Sort fibers by length (long to short)
 - 5: **for** $k \leftarrow 1$ **to** N **do**
 - 6: **for** $m \leftarrow 1$ **to** m_{max} **do**
 - 7: Update the fiber state (equations (3.8) and (3.9))
 - 8: Check the inter-fiber distances with the already accepted fibers
 - 9: **if** no collision is detected **then**
 - 10: Accept updated fiber
 - 11: Exit loop
 - 12: **else if** $m = m_{\text{max}}$ **then**
 - 13: Exit program (microstructure generation failed)
-

3.3. Control of the second order fiber orientation tensor

We are interested in the effect of the shaking procedure (3.9) on the fiber orientation tensors of order l . Recall that the volume-weighted fiber orientation tensors of l th-order for a finite number of fibers are defined via equation (2.4). Suppose the fibers follow the shaking procedure (3.9) and ignore the non-interpenetration condition. Then, the empirical fiber orientation tensors compute as

$$\mathbb{A}_{(l)} = \frac{1}{L_{\text{total}}} \sum_{k=1}^N L_k p_k(\theta_i(\xi_\theta), \varphi_i(\xi_\varphi))^{\otimes l} \quad (3.11)$$

with the additional information on the initial direction \mathbf{e}_i of each fiber. To understand this formula more thoroughly, we consider the continuum limit as the number of fibers N goes to infinity. A specific direction $p(\theta_i(\xi_\theta), \varphi_i(\xi_\varphi))$ depends on the realizations ξ_θ and ξ_φ of the normal distribution $\mathcal{N}(0, 1/3)$. Hence, an integration over the realizations ξ_θ and ξ_φ is necessary to include all directions on the unit sphere in the

computation of $\mathbb{A}_{(l)}^c$. We are led to the result

$$\mathbb{A}_{(l)}^c = \int_{-\infty}^{\infty} \int_{-\infty}^{\infty} \left[\tilde{a}_1^r p(\theta_1(\xi_\theta), \varphi_1(\xi_\varphi))^{\otimes l} + \tilde{a}_2^r p(\theta_2(\xi_\theta), \varphi_2(\xi_\varphi))^{\otimes l} \right] \psi(\xi_\theta) \psi(\xi_\varphi) d_\theta d_\varphi, \quad (3.12)$$

$$\psi(\xi) = \sqrt{\frac{3}{2\pi}} e^{-3/2\xi^2}, \quad \xi \in \mathbb{R}.$$

The two additive terms in the brackets account for the shaken directions of the two initial directions. As their influence on the computed fiber orientation tensor depends on their volume fractions, the two terms are weighted by the parameters \tilde{a}_1^r and \tilde{a}_2^r , which denote the realized eigenvalues of the initial step. The latter may feature deviations in respect to the prescribed initial eigenvalues due to sampling of the fiber lengths. Independently from its initial direction, the probability of a shaken direction is computed by multiplying the probability of the realizations ξ_θ and ξ_φ . Therefore, the function $\psi(\xi)$ is used representing the probability density function for the normal distribution $\mathcal{N}(0, 1/3)$. Notice that for the probability of the realizations ξ_θ and ξ_φ is accounted in an uncoupled way as Li et al. [27] assume independent shaking procedures for the angles θ_i and φ_i , see Eq. (3.9).

Li et al. [27] select the shaking parameters $\Delta\theta$ and $\Delta\varphi$ by trial and error. However, the computed fiber orientation tensor of second order \mathbb{A}^c only equals the prescribed tensor \mathbb{A} for a special parameter selection. Hence, for general fiber orientation the selection by trial and error leads to errors in the fiber orientation state of the generated microstructures. With the insight of the computed fiber orientation tensors at hand (3.12), we require that the computed tensor \mathbb{A}^c equals the prescribed tensor \mathbb{A} . Therefore, the shaking parameters $\Delta\theta$ and $\Delta\varphi$ are computed instead of selecting them by trial and error.

3.3.1. Computing the shaking parameter $\Delta\theta$

To match the third eigenvalue of the computed second-order fiber orientation tensor \mathbb{A}^c with the prescribed tensor \mathbb{A} , the condition

$$\begin{aligned} a_3 &\stackrel{!}{=} \int_{-\infty}^{\infty} \left[\tilde{a}_1^r p_3(\theta_1(\xi_\theta))^2 + \tilde{a}_2^r p_3(\theta_2(\xi_\theta))^2 \right] \psi(\xi_\theta) d_\theta \\ &= \int_{-\infty}^{\infty} \cos\left(\frac{\pi}{2} + \Delta\theta \xi_\theta\right)^2 \psi(\xi_\theta) d_\theta \end{aligned} \quad (3.13)$$

must hold. The latter equation involves only the single unknown $\Delta\theta$. As all fibers start in a planar setup with $\tilde{\theta}_i = \pi/2$, the two orthogonal layers are considered in a single term. We use the relationship between the trigonometrical functions to shorten the expression to

$$a_3 \stackrel{!}{=} \int_{-\infty}^{\infty} \sin(\Delta\theta \xi_\theta)^2 \psi(\xi_\theta) d_\theta. \quad (3.14)$$

Recasting equation (3.14) as optimization problem

$$\min_{\Delta\theta \in \mathbb{R}} \text{abs} \left(\int_{-\infty}^{\infty} \sin(\Delta\theta \xi_\theta)^2 \psi(\xi_\theta) d_\theta - a_3 \right), \quad (3.15)$$

we obtain the shaking parameter $\Delta\theta$ through a one-dimensional optimization procedure.

3.3.2. Computing the shaking parameter $\Delta\varphi$

The first and the second eigenvalue of the prescribed second order fiber orientation tensor are obtained by scaling the eigenvalues of the initial microstructure to consider that the third eigenvalue is set to zero:

$$a_1 = (1 - a_3) \tilde{a}_1 \quad \text{and} \quad a_2 = (1 - a_3) \tilde{a}_2. \quad (3.16)$$

As in Eq. (3.16), we split up the first eigenvalue of the tensor \mathbb{A}^c into two parts:

$$a_1 \stackrel{!}{=} (1 - a_3) \int_{-\infty}^{\infty} \left[\tilde{a}_1^r \cos(\Delta\varphi \xi_\varphi)^2 + \tilde{a}_2^r \sin(\Delta\varphi \xi_\varphi)^2 \right] \psi(\xi_\varphi) d_\varphi. \quad (3.17)$$

A derivation of Eq. (3.17) is given in Appendix.

Let us compare equation (3.16) and (3.17), then we observe that the integral in Eq. (3.17) must equal the initial orientation tensor component \tilde{a}_1 to obtain the prescribed eigenvalue a_1 :

$$\tilde{a}_1 \stackrel{!}{=} \int_{-\infty}^{\infty} \left[\tilde{a}_1^r \cos(\Delta\varphi \xi_\varphi)^2 + \tilde{a}_2^r \sin(\Delta\varphi \xi_\varphi)^2 \right] \psi(\xi_\varphi) d_\varphi. \quad (3.18)$$

This condition always holds, for the special case with equal eigenvalues $\tilde{a}_1 = \tilde{a}_2$ and an exactly realized initial fiber orientation tensor $\tilde{a}_1^r = \tilde{a}_1$:

$$\tilde{a}_1 \stackrel{!}{=} \tilde{a}_1 \int_{-\infty}^{\infty} \left[\cos(\Delta\varphi \xi_\varphi)^2 + \sin(\Delta\varphi \xi_\varphi)^2 \right] \psi(\xi_\varphi) d_\varphi = \tilde{a}_1. \quad (3.19)$$

Indeed, the parameter $\Delta\varphi$ may be selected freely without changing the computed fiber orientation tensors. Besides this special case, the condition as defined in Eq. (3.17) cannot hold. To handle this problem, two varying shaking parameters $\Delta\varphi_{1,2}$ for the initial directions have to be defined, i.e., the fibers shake with different intensity. Then, the equation

$$\tilde{a}_1 \stackrel{!}{=} \int_{-\infty}^{\infty} \left[\tilde{a}_1^r \cos(\Delta\varphi_1 \xi_\varphi)^2 + \tilde{a}_2^r \sin(\Delta\varphi_2 \xi_\varphi)^2 \right] \psi(\xi_\varphi) d_\varphi. \quad (3.20)$$

may be solved. Therefore, one parameter is set as shaking parameter – we choose $\Delta\varphi_2$ – which is selected by trial and error. The second parameter – we choose $\Delta\varphi_1$ – is identified via the optimization problem

$$\min_{\Delta\varphi_1 \in \mathbb{R}} \text{abs} \left(\int_{-\infty}^{\infty} \left[\tilde{a}_1^r \cos(\Delta\varphi_1 \xi_\varphi)^2 + \tilde{a}_2^r \sin(\Delta\varphi_2 \xi_\varphi)^2 \right] \psi(\xi_\varphi) d_\varphi - \tilde{a}_1 \right). \quad (3.21)$$

Notice that the optimization problem (3.21) is applicable for all cases. For the special case with equal eigenvalues and an exactly realized initial fiber orientation tensor, the parameter $\Delta\varphi_1$ equals the chosen parameter $\Delta\varphi_2$.

3.3.3. Implementation and workflow to determine the shaking parameters

Let us focus on the workflow for computing the shaking parameters $\Delta\theta$ and $\Delta\varphi_1$ which derive from the optimization problems (3.15) and (3.21). For solving these problems, we need the shaking parameter $\Delta\varphi_2$, as well as the orientation tensors \mathbb{A} , $\tilde{\mathbb{A}}$ and $\tilde{\mathbb{A}}^r$ as input. As the orientation tensor $\tilde{\mathbb{A}}^r$ is only available after the initial placement, we compute the shaking parameters $\Delta\theta$ and $\Delta\varphi_1$ as part of the preprocessing of the shaking step – subsequent to the initial step.

For the numerical implementation of the optimization problems (3.15) and (3.21), we use Python-integrated numerical integration and optimization tools. As limits for the corresponding integrals, we select the 99.99994%-confidence interval of the normal distribution $\mathcal{N}(0, 1/3)$:

$$\xi_{\min} = -5\sigma = -5\frac{\sqrt{3}}{3} \quad \text{and} \quad \xi_{\max} = 5\sigma = 5\frac{\sqrt{3}}{3}. \quad (3.22)$$

3.4. Single and multiple orientation shaking

The procedure of changing the fiber direction impacts the time efficiency, the achievable volume fraction as well as the realized fiber

orientation tensors. We investigate two types of shaking to study the differences. For the first protocol, which we call *multiple orientation shaking*, the fiber direction is updated recursively for every attempt. More precisely, the new shaking step is added to the initial angles of the fiber, see Eq. (3.9). By repeatedly changing the fiber direction, a faster microstructure generation is possible and higher volume fractions can be achieved. However, the prescribed fiber orientation state is not accurately realized.

In previous studies [52,53] it turns out that the fiber orientation influences the mechanical properties significantly. Hence, with more accurate fiber orientations in mind, we consider *single orientation shaking* as our second protocol. In this scenario, the angles are computed only once for every fiber before the first shaking attempt starts. After shaking the angles, the sampled direction p_k of every fiber is corrected to fulfill the fiber-orientation tensor of fourth order \mathbb{A}^c obtained by Eq. (3.12). To be more precise, we apply the iteration scheme introduced by Mehta and Schneider [31], see Alg. 2. The prefactor t is used to account for the influence of the fiber lengths on the volume-weighted fiber orientation tensor.

Although the procedure leads to a higher fidelity, it also increases the runtime and decreases the achievable volume fraction as it is not possible to change the direction during the shaking procedure. To compensate for this effect, we introduce the following idea. Suppose there is a fiber which could not be placed after a critical number m_{crit} . Then, we allow the k th-fiber to change its fiber direction in every attempt — similar to multiple orientation shaking. The critical number of attempts is chosen to depend on the maximum number of attempts m_{max} and the mean number of attempts of the previous ten percent of the fibers $\bar{m}_{10\%}$. As we update the fibers in order of descending fiber length, the volume-weighted fiber orientation tensor is mostly affected by the first fibers. To ensure a stable control of the fiber orientation state, we choose a higher critical number of attempts for the first thirty and last two percent of the N fibers:

$$m_{crit}(k) = \begin{cases} 0.1 m_{max}, & \text{if } k < 0.30 N, \\ m_{max}, & \text{if } k > 0.98 N, \\ \min(\max(1.5 \bar{m}_{10\%}, 1000), 0.1 m_{max}) & \text{else.} \end{cases} \quad (3.23)$$

By changing the presampled direction of the fiber, we influence the fiber orientation state. To compensate for this error, the presampled directions of the remaining (not updated) fibers are corrected again. For this reason, we adapt the factor t to take into account that the directions of the already updated fibers do not change:

$$t = (N - k) \left(\sum_{i=1}^k L_i \right) \left(\sum_{i=k+1}^N L_i \right)^{-2}. \quad (3.24)$$

If a correction is not possible, the k th-fiber will be shaken again starting from its last corrected direction with

$$p_k \leftarrow \frac{p_k + \Delta p}{\|p_k + \Delta p\|}, \quad \Delta p \hat{=} [\xi_{\Delta p_1} \quad \xi_{\Delta p_2} \quad \xi_{\Delta p_3}]^T. \quad (3.25)$$

The parameters $\xi_{\Delta p_1}$, $\xi_{\Delta p_2}$ and $\xi_{\Delta p_3}$ are realizations of the normal distribution $\mathcal{N}(0, g)$ using the parameter g to control the intensity of changing the direction. We choose an initial value of $g = 1/3$ for every fiber. If a correction is not accepted repeatedly, we will decrease the parameter with $g \leftarrow \max(g/1.5, 0.001)$.

In Alg. 3, a pseudo-code for the OCS method with single orientation shaking is provided.

4. Computational investigations

4.1. Setup

The presented algorithm is implemented in Python with Cython extensions. The collision checks between the fibers are parallelized with

Algorithm 2: Orientation correction (Mehta and Schneider [31])

```

1: while  $\|\mathbb{A}^c - \mathbb{A}^r\| > \|\mathbb{A}^c\| \cdot \text{error}$  do
2:    $\mathbb{A}^r = \frac{1}{L_{total}} \left[ \sum_{i=1}^N L_i p_i \otimes p_i \otimes p_i \otimes p_i \right]$ 
3:    $t \leftarrow 1/L_{mean}$ 
4:   for  $i \leftarrow 1$  to  $N$  do
5:      $\nabla_{p_i} f = (\mathbf{1} - p_i \otimes p_i) ((\mathbb{A}^c - \mathbb{A}^r) [p_i \otimes p_i \otimes p_i])$ 
6:      $p_i \leftarrow \frac{p_i + L_i t \nabla_{p_i} f}{\|p_i + L_i t \nabla_{p_i} f\|}$ 

```

Algorithm 3: OCS method with single orientation shaking

```

1: Initial Step
2: Arrange fibers in orthogonal layers according to  $\phi$ ,  $\rho_{\lambda, \beta}(L_k)$ ,  $\tilde{\mathbb{A}}$  and  $Q$ 
3: Shaking Step
4: Sort fibers by length (long to short)
5: Update the directions of all fibers (equation (3.9))
6: Correct the directions of all fibers (Alg. 2)
7: for  $k \leftarrow 1$  to  $N$  do
8:   for  $m \leftarrow 1$  to  $m_{max}$  do
9:     Update the fiber midpoint (equation (3.8))
10:    if  $m > m_{crit}(k)$  then
11:      if correction failed in the previous attempt then
12:        Update the fiber direction (equation (3.25))
13:      else
14:        Update the fiber direction (equation (3.9))
15:    Check the inter-fiber distances with the already accepted fibers
16:    if no collision is detected then
17:      if  $m > m_{crit}(k)$  then
18:        Correct the directions of the unshaken fibers (Alg. 2 with equation (3.24))
19:        if correction is successful then
20:          Accept updated fiber
21:          Exit loop
22:      else
23:        Accept updated fiber
24:        Exit loop
25:    else if  $m = m_{max}$  then
26:      Exit program (microstructure generation failed)

```

OpenMP. The runtimes for the microstructure generation are recorded on a desktop computer with a 8-core Intel i7 CPU and 64 GB RAM.

For computing the effective elastic properties, we use FFT-based computational homogenization software [54,55] with discretization on a staggered grid [56] and a conjugate gradient solver [57,58] terminated at a relative tolerance of 10^{-5} . For more details, we refer to the review article [59]. The effective elasticity tensor is computed based on six independent load cases. As the microstructures are orthotropic on average, we report on the effective orthotropic engineering constants. These are computed from the full effective elastic tensor in a postprocessing step [60,61].

We consider a polyamide 6.6 matrix, reinforced by E-glass fibers with the isotropic elastic parameters listed in Table 1, obtained by Hessman et al. [35]. For our studies, we select as our reference setup fibers with a diameter of $D = 10 \mu\text{m}$ and Weibull-distributed lengths with (volume-weighted) mean $m = 200 \mu\text{m}$ and standard deviation

Table 1
Material properties for the PA66 matrix and the E-glass fibers [35].

E-glass fibers			PA66 matrix		
E	=	72.0 GPa	E	=	3.0 GPa
ν	=	0.22	ν	=	0.40

Table 2
Used algorithmic parameters.

α	β	$\Delta\varphi_2$	m_{\max}
4	2	$3\pi/8$	10^7

$s = 80 \mu\text{m}$. We quantify the anisotropy of the microstructure in a unified way using the fiber orientation tensor of second order \mathbf{A} . A material with an isotropic fiber orientation is represented by the fiber orientation tensor $\mathbf{A} \hat{=} \text{diag}(1/3, 1/3, 1/3)$. Thus, the deviation of the fiber orientation tensor from this diagonal state represents a convenient measure of anisotropy. Moreover, the class of anisotropy may be read off the fiber orientation tensor. For instance, the fiber orientation tensors representing the class of transversely isotropic materials with polar direction e_1 read as

$$\mathbf{A} \hat{=} \text{diag}(a, b, b) \quad \text{with} \quad b = \frac{1-a}{2} \quad \text{and} \quad a \in [0, 1], \quad (4.1)$$

where we drop the sorting of the eigenvalues in the diagonal matrix \mathbf{A} for notational clarity. We correct the fiber directions in the procedure with single orientation shaking until the relative error of the fiber-orientation tensor of fourth order is lower than 10^{-5} . To avoid excessively high stresses between close fibers, we choose 20% of the fiber diameter, i.e., $2 \mu\text{m}$, as the minimum inter-fiber distance. The selected shaking parameters and the maximum number of attempts are listed in Table 2. Previous studies showed [6,7] that periodization of non-periodic media in combination with periodic boundary conditions leads to the lowest errors between the computed apparent stiffness and the desired effective stiffness for a given unit-cell size. According to these results, we generate periodic microstructures and use periodic boundary conditions for the displacement fluctuation to decrease the size of the RVEs.

4.2. On using the semi-analytic shaking parameter estimation

In this section, we investigate the difference in the computed and realized fiber orientation tensors by using identical parameter $\Delta\varphi_1 = \Delta\varphi_2$ for both orthogonal layers and computing the parameter $\Delta\varphi_1$ separately (3.21). For the study, we restrict to four volume fractions ϕ_i and five different fiber orientation tensors $\mathbf{A}_j \hat{=} \text{diag}(t_j, 0.98 - t_j, 0.02)$, see Table 3.

Let us start by comparing the computed fiber orientation tensors obtained via evaluating equation (3.12). Using the computation of parameter $\Delta\varphi_1$ leads to coinciding tensors \mathbf{A}^c and \mathbf{A} by construction (3.21). Hence, no error in the fiber orientation state is induced by the semi-analytic parameter estimation. In contrast, a difference between the tensors occurs for a parameter selection $\Delta\varphi_1 = \Delta\varphi_2$, see Table 4, in general. Notice that the prediction only depends on the shaking parameter $\Delta\varphi_2$ and is independent of the volume fraction. We observe that for mainly-planar isotropic microstructures the absolute error is zero. In this special case, the assumption of equal shaking parameters $\Delta\varphi_1 = \Delta\varphi_2$ does not infer an additional error, in agreement with the theoretical prediction (3.19). With increasing alignment of the fibers, the error intensifies and the maximum error is realized for the orientation state \mathbf{A}_5 with an absolute deviation of 0.341. Hence, it turns out that selecting equal shaking parameters $\Delta\varphi_i$ for both initial directions leads to a significant error in the computed fiber orientation tensors.

To compare this results with the realized fiber orientation tensors, we generated ten microstructures for every case of the study. For the

Table 3
Considered volume fractions ϕ_i and parameters t_j .

ϕ_1	ϕ_2	ϕ_3	ϕ_4	t_1	t_2	t_3	t_4	t_5
5%	10%	15%	20%	0.49	0.59	0.69	0.79	0.89

Table 4
Computed fiber orientation tensor \mathbf{A}_j^c with $\Delta\varphi_1 = \Delta\varphi_2$.

	$(\mathbf{A}_j^c)_{11}$	$(\mathbf{A}_j^c)_{22}$	$(\mathbf{A}_j^c)_{33}$	$\ \mathbf{A}_j^c - \mathbf{A}_j\ $
\mathbf{A}_1	0.490	0.490	0.020	0.000
\mathbf{A}_2	0.530	0.450	0.020	0.085
\mathbf{A}_3	0.569	0.411	0.020	0.171
\mathbf{A}_4	0.609	0.371	0.020	0.256
\mathbf{A}_5	0.649	0.331	0.020	0.341

process of changing the direction, we use the multiple orientation shaking protocol resulting in a new direction in every attempt. We choose a cubic cell-size with dimension $Q_i = 500 \mu\text{m}$ representing the 99.98%-quantile of the prescribed fiber length distribution. Hence, most of the fibers are smaller than an edge length.

For the lowest volume fraction of 5%, the observed errors transfer to the mean of the realized fiber orientation states with low discrepancy, see Fig. 5(a) for the component $(\mathbf{A}_j^c)_{11}$. The discrepancy is caused by sampling the direction of a fiber multiple times as result of detected inter-fiber collisions. Hence, the prescribed fiber orientation distribution is not realized exactly. For higher volume fractions, the deviation is increasing, as inter-fiber collisions are detected more frequently.

We notice that the deviation leads to an increasing mean of the component $(\mathbf{A}_j^c)_{11}$ for the orientation tensors \mathbf{A}_2 to \mathbf{A}_5 . This tendency is caused by the preference of the fibers to arrange in more aligned states with increasing fiber volume fraction, also observed in previous studies [62,63]. For the mainly-planar isotropic orientation tensor \mathbf{A}_1 , the fiber orientation state does not feature a preferred direction. Hence, the mean value of the component $(\mathbf{A}_1^c)_{11}$ does not change systematically. As a result of the tendency to arrange in more aligned states, the absolute error $\|\Delta\mathbf{A}_j\| = \|\mathbf{A}_j^c - \mathbf{A}_j\|$ ($j = 2, \dots, 5$) increases for higher volume fractions with computation of the parameter $\Delta\varphi_1$, see Fig. 5(b). In contrast, the error decreases for equal parameters $\Delta\varphi_{1,2}$ as the underestimation of the component $(\mathbf{A}_j^c)_{11}$ ($j = 2, \dots, 5$) is compensated. However, for the orientation state \mathbf{A}_5 , even for the highest volume fraction of 20%, the absolute error is 0.16 with equal shaking parameters, whereas, with computing the parameter $\Delta\varphi_1$, it is 0.06. Due to the lower errors resulting for the fiber orientation states \mathbf{A}_j ($j = 2, \dots, 5$), we conclude that computing the parameter $\Delta\varphi_1$ is an essential factor for achieving reliable results.

Last but not least, we focus on the differences in the runtime. Solving the problem (3.21) is conducted as part of the preprocessing of the shaking step and has no significant influence on the runtime. During the shaking step the runtime slightly increases for equal parameters $\Delta\varphi_1 = \Delta\varphi_2$ as it is computationally more expensive to generate microstructures which are closer to the mainly-planar isotropic state.

As a result of the smaller errors in the fiber orientation state, the subsequent investigations use a computed parameter $\Delta\varphi_1$.

4.3. On the difference between single and multiple orientation shaking

In the previous section, significant errors in the fiber orientation states, even with computed $\Delta\varphi_1$, are observed due to the multiple orientation shaking in case of inter-fiber collisions. As the effective mechanical properties of a composite strongly depend on the orientation state of the reinforcing fibers, it is essential to match the prescribed fiber orientation tensors accurately. To focus on this objective, we additionally investigate the procedure of single orientation shaking, which leads to matching fiber orientation tensors:

$$\mathbf{A} = \mathbf{A}^c = \mathbf{A}^r \quad \text{and} \quad \mathbf{A}^c = \mathbf{A}^r. \quad (4.2)$$

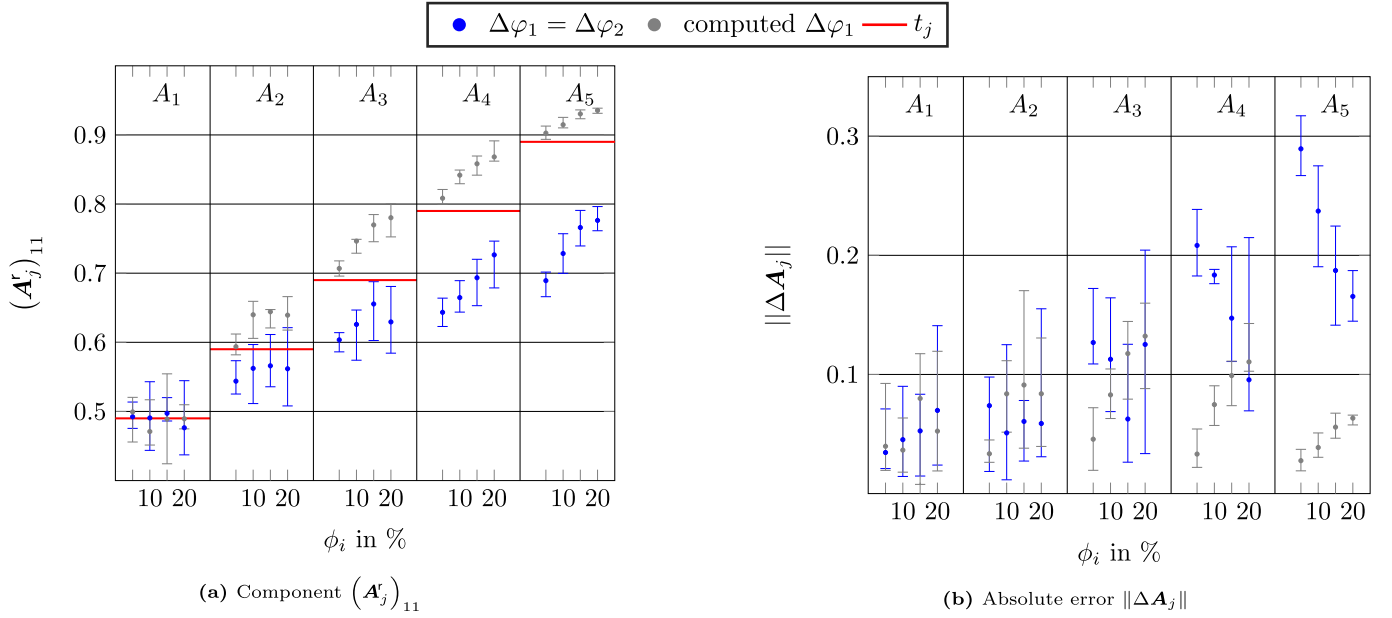


Fig. 5. Comparison of the realized fiber orientation tensor A_j^r between using $\Delta\phi_1 = \Delta\phi_2$ and computing $\Delta\phi_1$ with Eq. (3.21) for five different prescribed fiber orientation tensors A_j .

We repeat the study from Section 4.2 for single orientation shaking and compare the results to multiple orientation shaking. Fig. 6(a) shows that the component $(A_j^r)_{11}$ equals the component t_j for all cases.

The price to pay for this increase in accuracy is an increase in runtime, see Fig. 6(b). For the mainly-planar isotropic case, the mean of the runtime is similar for both procedures and only the high whisker is larger for multiple orientation shaking. For the fiber orientation states A_j ($j = 2, \dots, 5$), the procedure of multiple orientation shaking leads to smaller runtimes as it permits the fibers to follow their natural, and computationally less expensive, tendency to more aligned orientation states. In contrast, single orientation shaking enforces the prescribed fiber orientation state which leads to a higher computational expense, in general. By taking the fiber orientation tensor A_3 and a volume fraction of 20% as example, the runtime is 149 s for multiple orientation shaking and 255 s for single orientation shaking, i.e., an increase by 71%.

Despite the increase in runtime, the microstructures are still generated in acceptable time. Hence, we use single orientation shaking throughout the next investigations to ensure reliable microstructures.

4.4. Study on the resolution and the RVE size

To compute precise effective properties, we need to investigate the necessary resolution and the RVE size leading to accurate results. For this purpose, we consider the fiber setup from the study in Section 4.2 and the material parameters of Table 1. We examine the extreme fiber orientation states $A_{1,5}$ and choose $\phi = 20\%$ as volume fraction.

In Fig. 7, the realized directions of two corresponding microstructures are represented by a pole figure. For a two-dimensional representation, a stereographic projection of the fiber directions into the plane with normal direction e_3 is used. Then, the angle θ of each fiber is represented by the parameter $r = \tan(\theta/2)$, see [64]. Notice that for this representation the angle φ is parameterized on the domain $[0, 2\pi)$ and θ on the domain $[0, \pi/2]$ using the periodic characteristic of the angles and the equivalent description of a fiber with direction p or $-p$. To represent the influence of a single fiber on the volume-weighted fiber orientation tensor, the color and size of the marks accounts for the fiber lengths. We observe that in Fig. 7(a) the fiber directions are

equally distributed in respect to the angle φ , but tend to the outer parts for the parameter r , which represent more planar orientation states. This corresponds to the mainly-planar isotropic characteristic of the fiber orientation tensor A_1 . In contrast, in Fig. 7(b) most directions are located near the horizontal line at $\varphi = 0$, representing the almost unidirectional fiber orientation tensor A_5 .

To compute the effective properties accurately, the resolution has to be sufficiently fine [58,65]. However, with smaller mesh size, the runtime for the computation of the effective properties is increasing. To balance these conflicting objectives, it is necessary to select a resolution leading to reasonable computational effort and sufficient accuracy. We select one of the ten microstructures generated in Section 4.3 for both fiber orientation tensors. We consider the voxel edge-lengths $4 \mu\text{m}$, $2 \mu\text{m}$ and $1 \mu\text{m}$ resolving a fiber with 2.5, 5 and 10 voxels per diameter, respectively. In Fig. 8, $(240 \mu\text{m})^3$ -extractions of the microstructures for varying mesh sizes are shown.

For the mainly-planar isotropic fiber orientation tensor A_1 , the fibers' directions feature no preference in the e_1 - e_2 -plane. Hence, the Young's moduli in e_1 - and e_2 -direction almost coincide for all three resolutions, see Table 5. Due to the dominant fiber arrangement in the e_1 - e_2 -plane, the Young's modulus in e_3 -direction is smaller. The same reason leads to a higher shear modulus G_{12} compared to the other two shear moduli. For a voxel edge-length $h = 4 \mu\text{m}$, the largest relative error – relative to the highest resolution – is obtained for the shear modulus G_{12} with 5.95%, decreasing to 2.38% for $h = 2 \mu\text{m}$. As we report on the approximated orthotropic engineering constants instead of the full effective elastic tensor, the orthotropic approximation error err_{orth} must be assessed to control the quality of the results. We observe that even for the coarsest resolution, the error is lower than two percent and decreases to a quarter percent for the finest resolution. For the almost aligned case, the Young's modulus E_1 exceeds the other moduli by at least a factor of two. Also it is affected the most by increasing the resolution. For the coarsest resolution, the relative error is 6.99% decreasing to 1.91% for $h = 2 \mu\text{m}$. Similar to the mainly-planar isotropic case, the approximation error is rather low and decreases to under one percent with $h = 2 \mu\text{m}$.

As an outcome of the resolution study, we choose a voxel edge-length of five voxels per diameter leading to a relative error below

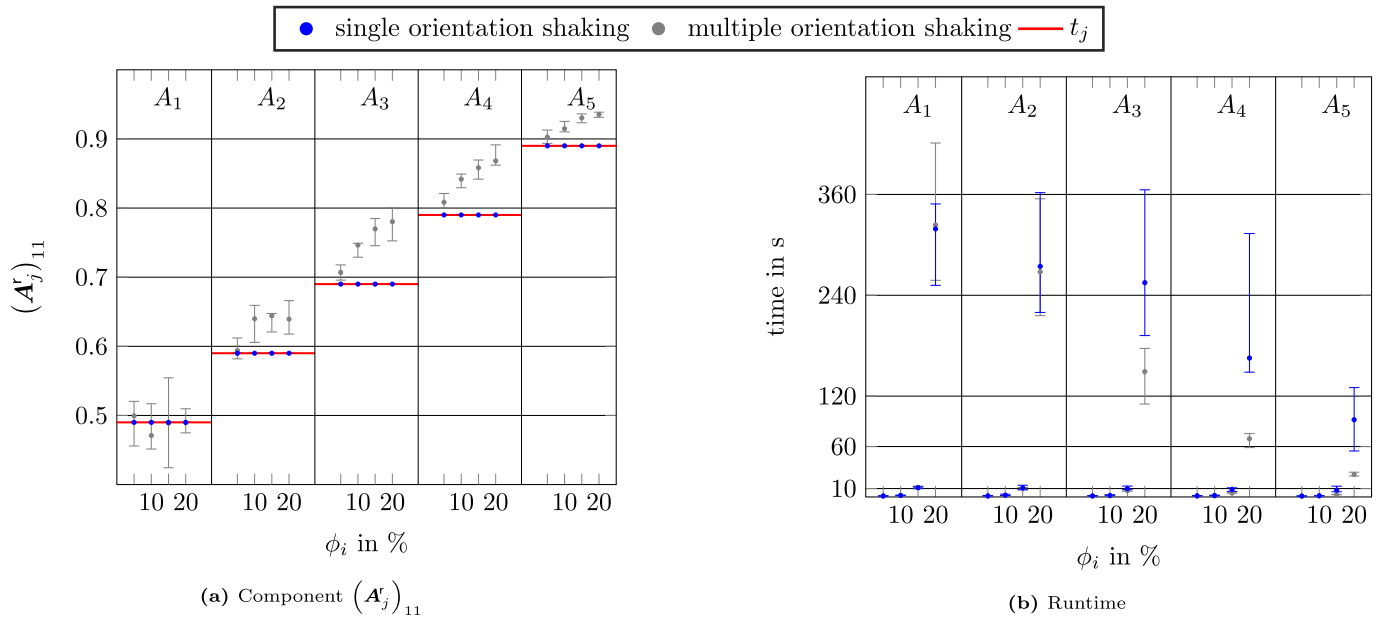


Fig. 6. Comparison of the realized fiber orientation tensor $(A_j^r)_{11}$ and the runtime between single and multiple orientation shaking for five different prescribed fiber orientation tensors A_j .

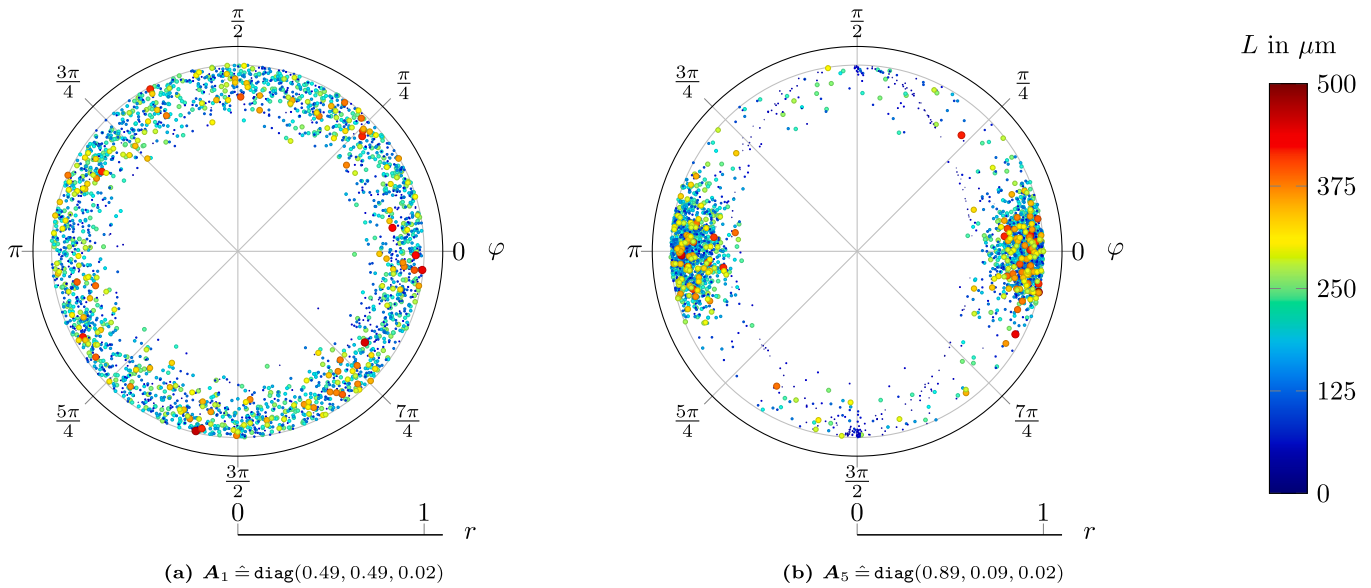


Fig. 7. Stereographic projection of the fiber directions of two realized microstructures for varying fiber orientation tensors.

Table 5

Approximated effective orthotropic engineering constants for three different resolutions and fiber orientation tensors $A_1 \hat{=} \text{diag}(0.49, 0.49, 0.02)$ and $A_5 \hat{=} \text{diag}(0.89, 0.09, 0.02)$.

	h μm	E_1 GPa	E_2 GPa	E_3 GPa	G_{23} GPa	G_{13} GPa	G_{12} GPa	err_{orth} %
A_1	4	6.59	6.61	5.16	1.78	1.78	2.46	1.91
	2	6.79	6.82	5.19	1.72	1.72	2.51	0.74
	1	6.86	6.89	5.18	1.68	1.68	2.52	0.25
A_5	4	10.25	5.07	4.90	1.69	1.86	1.98	1.48
	2	10.81	5.09	4.90	1.63	1.80	1.94	0.63
	1	11.02	5.08	4.89	1.59	1.77	1.91	0.30

three percent and an orthotropic error below one percent. This selection confirms the results of previous resolution studies [29,66].

After identifying the necessary resolution, we turn our attention to the required size of a representative volume element. As a result of the

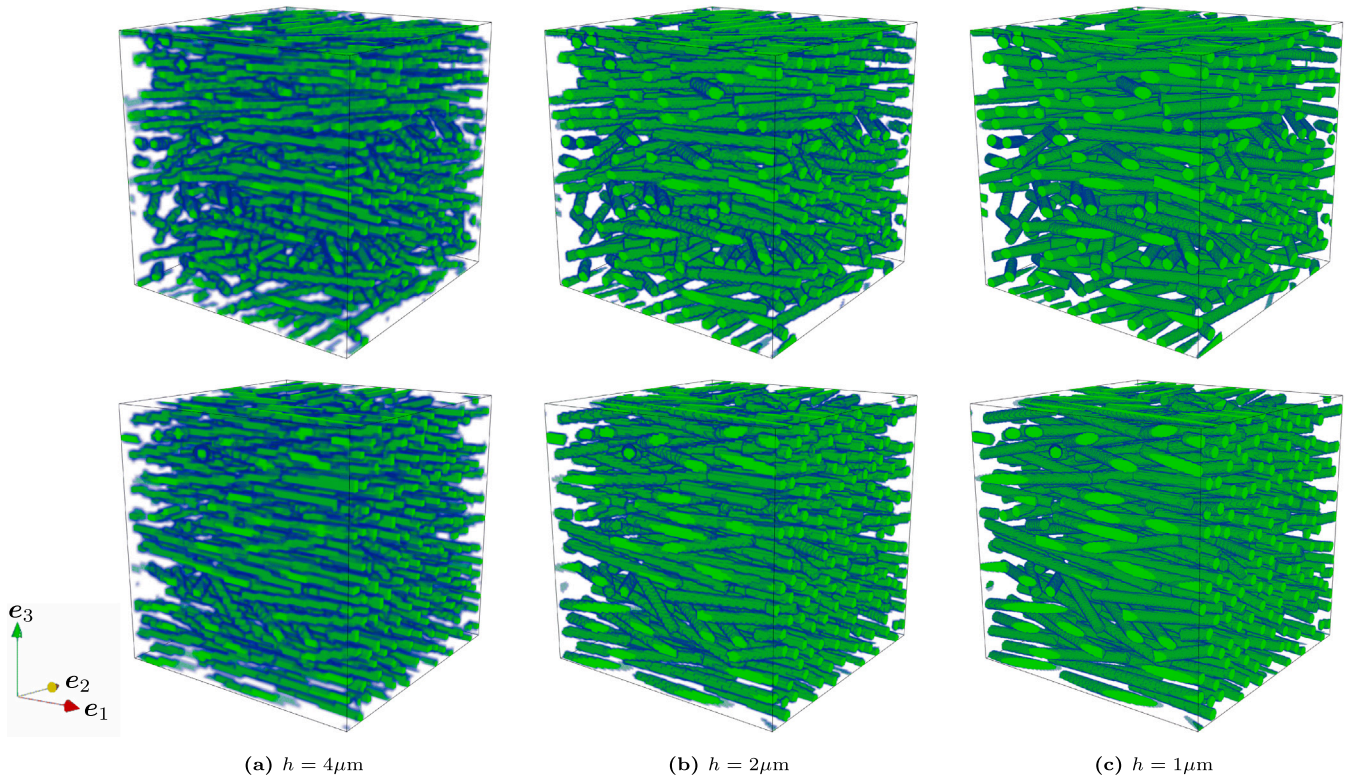


Fig. 8. $(240 \mu\text{m})^3$ -extractions of microstructures with three different voxel-edge lengths and fiber orientation tensors $A_1 \hat{=} \text{diag}(0.49, 0.49, 0.02)$ (top) and $A_5 \hat{=} \text{diag}(0.89, 0.09, 0.02)$ (bottom).

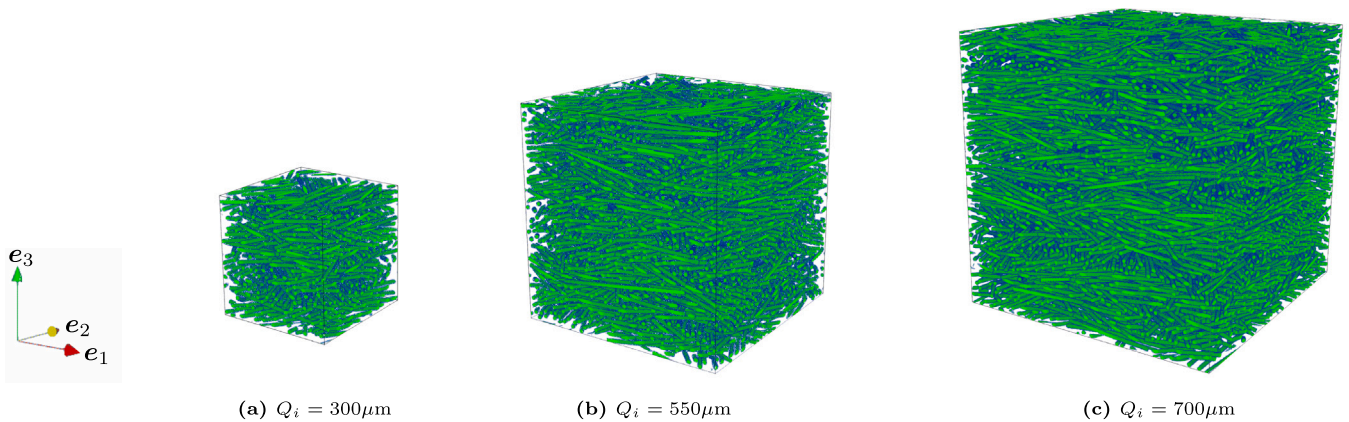


Fig. 9. Generated microstructures with the second-order fiber orientation tensor $A_1 \hat{=} \text{diag}(0.49, 0.49, 0.02)$ for three different cubic cell-sizes.

manufacturing process and the material, fiber-reinforced composites are characterized by randomness in, e.g., their realized fiber lengths, fiber directions and fiber positioning. Consequently, the computed elastic properties are random variables, as well. However, the effective properties as deterministic descriptors are only obtained on cells of sufficient size, the so-called representative volume elements (RVEs) [6, 67,68].

When working with cells of finite size, the incurring error naturally decomposes into two terms. The standard deviation of the apparent properties is called random error and quantifies their dispersion [6,69]. This error may be reduced by averaging multiple samples on cells of equal size [70,71]. The second, so-called systematic, error equals the difference of the mean of the apparent properties and the effective elastic properties [6,69]. We monitor this error by increasing the unit cell size and observing to what extent the mean is changing. In case of

sufficiently small random and systematic errors, the investigated unit cell size is usable for a representative volume element.

For reducing the representativity errors, we enforce a high accuracy regarding the prescribed properties, for example the fiber length distribution and the fiber orientation state. According to previous studies, periodic boundary conditions leads to lower random and systematic errors as well [7,13]. For these reasons, we expect rather low representativity errors.

In the following RVE study, we choose cubic cell-sizes with dimensions $Q_i = 300 \mu\text{m}$, $Q_i = 550 \mu\text{m}$ and $Q_i = 700 \mu\text{m}$ and the previously identified resolution $h = 2 \mu\text{m}$. For the fiber orientation tensors A_1 and A_5 , we consider ten realizations for every unit cell size. Fig. 9 shows generated microstructures for the orientation state A_1 and the three cell sizes. To quantify the representativity of the unit cells, we compute the empirical mean and the standard deviation of the approximated

Table 6

Approximated effective orthotropic engineering constants for three different cubic cell-sizes and fiber orientation tensors $\mathbf{A}_1 \doteq \text{diag}(0.49, 0.49, 0.02)$ and $\mathbf{A}_5 \doteq \text{diag}(0.89, 0.09, 0.02)$.

	Q_i μm	E_1 GPa	E_2 GPa	E_3 GPa	G_{23} GPa	G_{13} GPa	G_{12} GPa	err_{orth} %
\mathbf{A}_1	300	6.90 ± 0.07	6.88 ± 0.05	5.22 ± 0.01	1.72 ± 0.00	1.72 ± 0.00	2.54 ± 0.01	0.79 ± 0.12
	550	6.83 ± 0.02	6.81 ± 0.02	5.19 ± 0.00	1.72 ± 0.00	1.72 ± 0.00	2.53 ± 0.00	0.96 ± 0.06
	700	6.82 ± 0.02	6.81 ± 0.02	5.19 ± 0.00	1.72 ± 0.00	1.72 ± 0.00	2.53 ± 0.00	0.94 ± 0.07
\mathbf{A}_5	300	10.86 ± 0.08	5.11 ± 0.04	4.91 ± 0.01	1.63 ± 0.00	1.81 ± 0.00	1.94 ± 0.01	0.63 ± 0.06
	550	10.88 ± 0.03	5.09 ± 0.01	4.91 ± 0.00	1.63 ± 0.00	1.81 ± 0.00	1.94 ± 0.00	0.63 ± 0.03
	700	10.88 ± 0.02	5.09 ± 0.01	4.91 ± 0.00	1.63 ± 0.00	1.81 ± 0.00	1.94 ± 0.00	0.63 ± 0.01

engineering constants, see Table 6. The orthotropic error err_{orth} is smaller than 1%, showing an adequate orthotropic approximation of the computed effective stiffness. We observe that the shear moduli are almost unaffected by changing the size of the unit cell. Also for the Young's moduli, the dispersion and the bias are rather low and decrease for an increasing unit cell size. The highest systematic error is computed for the Young's modulus E_1 in the mainly-planar isotropic fiber arrangement. Compared to the large-scale modulus a relative error of 1.17% occurs for $Q_i = 300 \mu\text{m}$, dropping to 0.15% for $Q_i = 550 \mu\text{m}$. The systematic error for the almost aligned case is even lower, not exceeding 0.5% for any engineering constant or unit cell size.

To sum up, the results confirm our expectation that combining periodic boundary conditions and higher accuracy of the descriptive parameters of the microstructure results in low representativity errors. In fact, even the smallest unit cell size $Q_i = 300 \mu\text{m}$ leads to acceptable errors for engineering applications.

4.5. Effective stiffness compared to the SAM algorithm

In this section, we compare the computed effective stiffness of microstructures generated with the Orientation Corrected Shaking method and the Sequential Addition and Migration (SAM) algorithm [29,31]. Therefore, we reproduce the results of the RVE study in Table 6 for microstructures generated by the SAM algorithm.

Already in previous studies [29,30,32], it is pointed out that the effective elastic properties are determined by the fiber orientation tensor of fourth order \mathbb{A} , i.e., prescribing the fiber orientation tensor of second order \mathbf{A} is not sufficient. For this reason, the presented OCS method as well as the SAM algorithm enforce a close match of the fiber orientation tensor of fourth order. However, in practice, only the fiber orientation tensor of second order is available and the additional information included in the fiber orientation tensor of fourth order is not known. For this reason, the fourth order fiber orientation tensor within the SAM algorithm is estimated by a closure approximation [25, 72–75]. In contrast, for the OCS method the previously presented intrinsic computation of higher-order fiber orientation tensors is applied, see Eq. (3.12).

Due to the lack of data, the choice of the closure approximation represents another parameter to be selected. Furthermore, as second-order fiber orientation tensors are either isotropic, transversely isotropic or orthotropic [61,76], closure approximations are restricted on these material symmetries as well [42].

In the following study, we investigate the influence of the chosen closure approximation on the computed effective stiffness. Therefore, we consider the intrinsic closure of the OCS method and, for the SAM algorithm, the exact closure (ACG) [77,78] as well as the maximum entropy closure (MEC) [32,79].

We choose $Q_i = 550 \mu\text{m}$ as cell size, following the results of the RVE study for the OCS method. In Mehta and Schneider [31] the necessary RVE size is investigated for the SAM algorithm, as well. It is shown that for a similar material the cell size $Q_i = 300 \mu\text{m}$ is already representative for engineering applications. Hence, we assume that the chosen cell size $Q_i = 550 \mu\text{m}$ is applicable for the SAM algorithm as RVE, especially as we consider even shorter fibers than Mehta and Schneider [31].

In Table 7, the results for both microstructure generators are shown. We observe that both random and orthotropic error are small for the effective stiffness based on the SAM algorithm, in the same manner as we observed for the OCS method. Hence, the chosen cell size is representative for both generators.

For the mainly-planar isotropic case, the computed moduli for the three closure approximations are comparable. Considering the shear moduli G_{23} and G_{13} , we even notice that all considered closures lead to almost the same results. The remaining moduli turn out to be close, as well.

The highest relative difference is computed for the shear modulus G_{12} between the OCS method and the exact closure with 3.95%. Higher differences are obtained by investigating the almost aligned case. Even for the shear moduli G_{23} and G_{13} , we observe remarkable differences with a maximum of 3.41% for G_{13} between the exact and the maximum entropy closure. Moreover, the Young's modulus in e_1 -direction E_1 differs by more than half a GPa, slightly more than six percent. Again, the highest relative difference is computed for G_{12} with 13.92%, which is about ten percent higher compared to the mainly-planar isotropic case. Bauer and Böhlke [80] study the influence of the exact and maximum entropy closure on the reconstructed fiber orientation distribution for planar fiber arrangement. Higher differences between the approximations are observed for increasing fiber alignment, corresponding to our results for the computed effective stiffness.

Let us focus on the almost unidirectional case to investigate the higher differences more thoroughly. In Fig. 10(a), the mean of the direction dependent Young's modulus with tensile directions in the e_1 - e_2 -plane is shown. For details on the computation of the direction dependent Young's modulus $E(\mathbf{p})$, we refer to, e.g., Böhlke and Brüggemann [64]. Notice that the computed effective stiffness, instead of its orthotropic approximation, is used for the computation of direction dependent Young's modulus. Via the visualization, it turns out that the shape of the Young's modulus almost coincides for the OCS method and the exact closure, whereas it differs for the maximum entropy closure, especially near the angle $\varphi = \pi/2$. By plotting the relative difference to the OCS method

$$\delta E(\mathbf{p}) = \frac{|E_{\text{OCS}}(\mathbf{p}) - E_{\text{ACG/MEC}}(\mathbf{p})|}{E_{\text{OCS}}(\mathbf{p})} \cdot 100\% \quad (4.3)$$

in Fig. 10(b), we observe that the highest relative differences are computed for the maximum entropy closure for planar tensile directions with angles near $\varphi = \pi/4$, corresponding to the result shown in Table 7. Additionally, the plot visualizes that the computed Young's moduli are not exactly orthotropic as the relative difference is not symmetric with respect to the vertical line at $\varphi = \pi/2$, see, e.g., the angles $\varphi = \pi/4$ and $\varphi = 3\pi/4$.

To conclude, it turns out that especially for the almost aligned orientation state the selection of the closure approximation influences the computed effective stiffness noticeably, i.e., up to 10% in this study. As all microstructures represent the prescribed tensors $\mathbf{A}_{1,5}$, it is not possible to decide which closure approximation performs best without additional data. For this reason, we emphasize the importance of including additional information on the fiber orientation state to reduce the uncertainty by selecting a closure approximation.

Table 7

Approximated effective orthotropic engineering constants of microstructures with fiber orientation tensors $\mathbf{A}_1 \hat{=} \text{diag}(0.49, 0.49, 0.02)$ and $\mathbf{A}_5 \hat{=} \text{diag}(0.89, 0.09, 0.02)$ generated with the OCS method and with the SAM algorithm (based on the exact (ACG) or on the maximum entropy closure (MEC)).

		E_1 GPa	E_2 GPa	E_3 GPa	G_{23} GPa	G_{13} GPa	G_{12} GPa	err_{orth} %
\mathbf{A}_1	OCS	6.83 ± 0.02	6.81 ± 0.02	5.19 ± 0.00	1.72 ± 0.00	1.72 ± 0.00	2.53 ± 0.00	0.96 ± 0.06
	ACG	7.02 ± 0.02	7.02 ± 0.01	5.32 ± 0.00	1.71 ± 0.00	1.71 ± 0.00	2.63 ± 0.00	1.06 ± 0.04
	MEC	6.98 ± 0.01	6.98 ± 0.01	5.27 ± 0.00	1.73 ± 0.00	1.73 ± 0.00	2.62 ± 0.00	1.01 ± 0.03
\mathbf{A}_5	OCS	10.88 ± 0.03	5.09 ± 0.01	4.91 ± 0.00	1.63 ± 0.00	1.81 ± 0.00	1.94 ± 0.00	0.63 ± 0.03
	ACG	11.04 ± 0.03	5.11 ± 0.00	5.00 ± 0.00	1.67 ± 0.00	1.76 ± 0.00	2.04 ± 0.00	0.68 ± 0.02
	MEC	10.41 ± 0.02	4.88 ± 0.00	4.96 ± 0.00	1.65 ± 0.00	1.82 ± 0.00	2.21 ± 0.00	0.78 ± 0.02

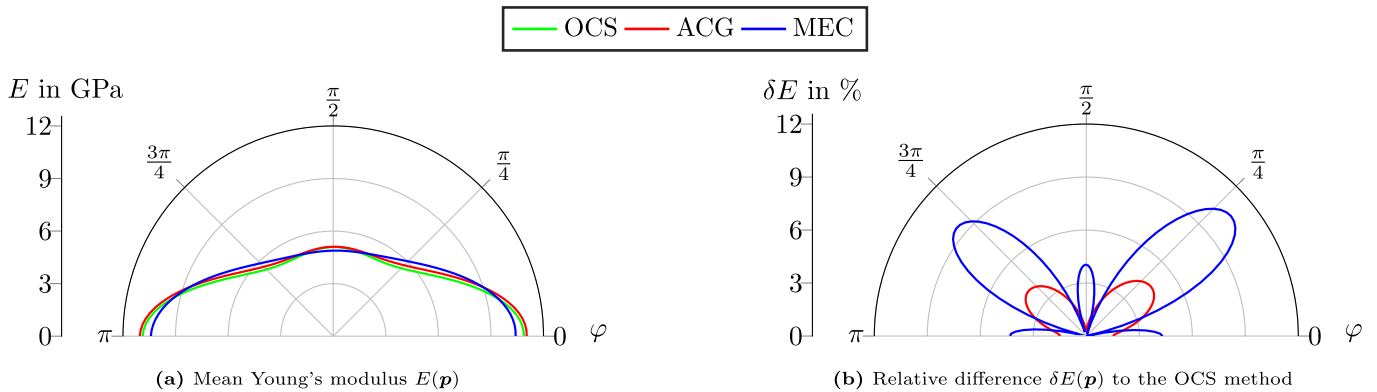


Fig. 10. Comparison of the computed mean Young's modulus in the e_1 - e_2 -plane of microstructures with fiber orientation tensor $\mathbf{A}_5 \hat{=} \text{diag}(0.89, 0.09, 0.02)$ generated with the OCS method and with the SAM algorithm (based on the exact closure (ACG) or on the maximum entropy closure (MEC)).

4.6. Application to a PA66GF35 material

In this section, we apply the OCS method to an injection molded PA66GF35 composite with experimental data provided by Hessman et al. [35,39]. The material is reinforced with fibers of $10 \mu\text{m}$ diameter, making up a volume fraction of $\phi = 19.3\%$. Mehta and Schneider [31] fit the measured length distribution [39] with a Weibull distribution, resulting in a volume-weighted mean $m = 332.16 \mu\text{m}$ and a standard deviation $s = 127.64 \mu\text{m}$ as distribution parameters. Concerning the fiber orientation state, a skin-core-skin distribution is observed which is typical for injection molded composites [81–83]. To analyze the influence of whether the layer structure is explicitly modeled or not, in analogy to Mehta and Schneider [31], we generate microstructures with a mean fiber orientation tensor

$$\mathbf{A}_{\text{mean}} \hat{=} \text{diag}(0.7855, 0.1962, 0.0183) \quad (4.4)$$

over the whole height as well as skin-core-skin layered microstructures with

$$\begin{aligned} \mathbf{A}_{\text{skin}} &\hat{=} \text{diag}(0.8602, 0.1227, 0.0171) \\ \mathbf{A}_{\text{core}} &\hat{=} \text{diag}(0.2255, 0.7424, 0.0321), \end{aligned} \quad (4.5)$$

where the core layer occupies one sixth of the total height. Both the fiber orientation data and the height of the core layer is extracted from Hessman et al. [35,39]. For a comparison with the results given by Mehta and Schneider [31], we choose the same cubic cell size $Q_i = 800 \mu\text{m}$, a resolution $h = 2 \mu\text{m}$ and consider ten realizations. The boundaries between the layers are characterized by a soft constraint forcing the midpoint of a fiber to be in its respective layer. In Fig. 11, generated mean and sandwich microstructures are shown. Taking a look at the sandwich microstructure in Fig. 11(b), we notice the different preferred directions of the fibers for the skin and core layers resulting from the prescribed fiber orientation tensors \mathbf{A}_{skin} and \mathbf{A}_{core} .

The computed Young's moduli in e_1 - and e_2 -direction are listed in Table 8. Mehta and Schneider [31] use the exact closure. In brackets the relative error of the computed Young's modulus compared to the experimental data is shown.

Considering the computed standard deviations, we obtain an insignificant random error for all generated microstructures. In fact, the standard deviation of the experiments is one order of magnitude higher. For the Young's modulus in e_1 -direction E_1 , we observe that by using the sandwich structure a close approximation to the experimental data for both microstructure generators is obtained. Using the mean data leads to an underestimation of the modulus E_1 with higher differences than the sandwich structure, up to 3.38% for the OCS method and 4.16% for the SAM algorithm. In contrast, the transverse Young's modulus E_2 for the mean data fits to the experimental data with high accuracy. However, the sandwich structure leads to a significantly overestimated modulus E_2 with relative errors of 8.18% for the OCS method and 5.09% for the SAM algorithm. For the transverse modulus, there is a remarkable difference between the microstructure generators.

Taking a look at the runtime, for the OCS method, the mean runtime to generate the microstructures is about 100 min for the mean structures and 110 min for the sandwich structures. In contrast, Mehta and Schneider [31] compute a runtime below two minutes for all generated microstructures. Notice that for this study a different desktop computer is used. The smaller runtime for the SAM algorithm is characteristic of collective-rearrangement methods, whereas the OCS method is a sequential insertion algorithm. Still, we observe that sequential insertion methods are capable of generating industrially relevant fiber microstructures with a reasonable computational effort, displaying a good agreement with experimental data.

5. Summary and conclusion

In this work, the Orientation Corrected Shaking method is presented based on the two-stage shaking algorithm by Li et al. [27] for generating microstructures with almost planar fiber arrangements. As extensions, we consider periodic boundary conditions and implement a scheme that works for general rectangular unit cells, in contrast to Li et al. [27]. Additionally, the realized fiber orientation states of the OCS method are investigated. Therefore, we uncover the hidden closure

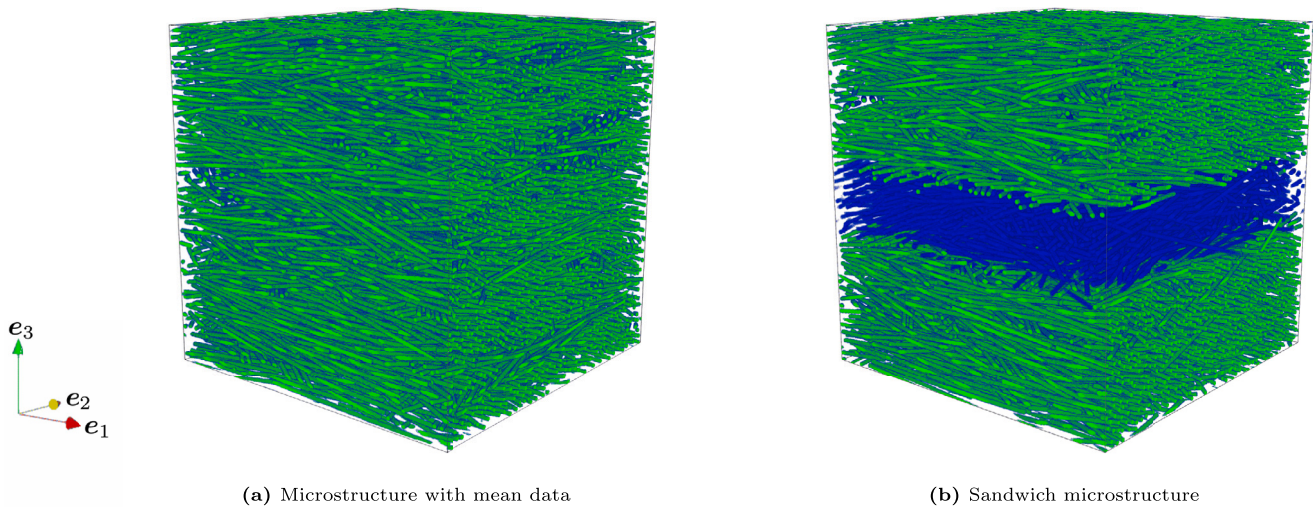


Fig. 11. Microstructures generated with mean data and with data for a sandwich structure according to Hessman et al. [35,39].

Table 8

Comparison of the experimental results [35] and the computed mechanical properties obtained by using the OCS method or the SAM algorithm [31] with exact closure.

	Experiments [35, Fig. 2]	Sandwich	Mean data	Sandwich [31, Tab. 5]	Mean data [31, Tab. 5]
E_1 in GPa	10.34 ± 0.4	10.17 ± 0.04 [1.64%]	9.99 ± 0.03 [3.38%]	10.42 ± 0.03 [0.77%]	9.91 ± 0.03 [4.16%]
E_2 in GPa	5.50 ± 0.1	5.96 ± 0.01 [8.18%]	5.47 ± 0.01 [0.55%]	5.78 ± 0.00 [5.09%]	5.56 ± 0.02 [1.09%]

structure by revealing an exact expression of the realized fiber orientation tensors of any order ignoring the non-penetration condition. With this insight at hand, we compute the shaking parameters $\Delta\theta$ and $\Delta\varphi_1$ directly instead of selecting them by trial and error. Last but not least, the procedure of single orientation shaking is presented to overcome inaccuracies during the shaking step as result of the non-penetration condition.

The computational investigations included in this work lead to the following conclusions:

- The influence of the semi-analytic shaking parameter estimation and of the procedure of single orientation shaking on the realized fiber orientation tensors is studied. It turns out that a combination of both strategies is necessary to match the fiber orientation state accurately. Otherwise, we observe significant errors for the fiber orientation tensor of second order, e.g., an absolute error of 34.1% in case of equal shaking parameters for both orthogonal layers and single orientation shaking.
- Due to the user-selected rectangular unit cell size of the OCS method, it is possible to investigate the necessary RVE size. The study reveals rather low random and systematic errors, even for the smallest unit cell rather. Additionally, a good approximation of the orthotropic engineering constants is observed. Hence, the OCS method leads to rather small representative volume elements. We emphasize that this is caused by the combination of periodic boundary conditions with an accurate realization of the fiber volume fraction, as well as the fiber length and orientation distributions.
- The computed effective stiffness of the intrinsic closure approximation of the OCS method is compared with the exact and maximum entropy closures implemented within the framework of the SAM [29,31] algorithm. We observe differences exceeding ten percent between the three approximation closures, although all microstructures represent the same fiber orientation tensors

of second order. Hence, it is confirmed that using only a fiber orientation of second order as input is not sufficient to describe a fiber-reinforced composite. To minimize uncertainties introduced by closure approximations, access to the full fiber orientation tensors of fourth order is necessary.

- Applying the OCS method to an injection molded PA66GF35 material with mean aspect ratio of 33 and volume fraction of 19.3%, shows the capability of generating microstructures for industrial produced materials. By comparing the computed effective stiffness to experimental data, a good coincidence of the longitudinal Young's moduli is observed, especially for the layered sandwich structure. Similar to the microstructures generated by the SAM algorithm based on the exact closure [31], the transverse Young's modulus is overestimated for the OCS method as well — by about 8%, which is still adequate for engineering accuracy. According to Mehta and Schneider [31], possible reasons for the differences are imprecise fiber orientation and length distributions due to the incomplete segmentation of the fibers during the analysis of the Micro-CT scan, the missing fiber orientation tensors of fourth order and the assumption of the fiber length distribution to be uniform for the entire microstructure.

To conclude, the numerical investigations show that the OCS method is capable of generating representative microstructures for industrial volume fractions and aspect ratios in reasonable time. The synthetic microstructures feature accurately realized properties, as volume fraction and fiber length and orientation distributions. Especially the representation of the fiber orientation state is improved significantly as we adapt the shaking step to account for an accurate realization of the fiber orientation tensor of fourth order. Hence, the generated microstructures are capable of representing the real microstructure adequately, which leads to a close match between experimental data and the results of computational homogenization. Last but not least, the extensions for a user-selected rectangular size of the unit cell and periodic boundary

conditions reduce the RVE sizes resulting in smaller runtimes for the microstructure generation and computational homogenization.

CRedit authorship contribution statement

Celine Lauff: Methodology, Software, Validation, Formal analysis, Investigation, Data curation, Writing – original draft, Writing – review & editing, Visualization, Project administration. **Matti Schneider:** Conceptualization, Methodology, Software, Resources, Data curation, Writing – review & editing, Supervision, Project administration, Funding acquisition. **John Montesano:** Conceptualization, Writing – review & editing, Supervision. **Thomas Böhlke:** Conceptualization, Methodology, Resources, Writing – review & editing, Supervision, Project administration, Funding acquisition.

Declaration of competing interest

The authors declare that they have no known competing financial interests or personal relationships that could have appeared to influence the work reported in this paper.

Data availability

The raw/processed data required to reproduce these findings cannot be shared at this time as the data also forms part of an ongoing study.

Acknowledgments

The personal communication with Zeyang Li is gratefully acknowledged. We thank the anonymous reviewers for their valuable comments which helped improve the manuscript. The research documented in this manuscript has been funded by the German Research Foundation (DFG), project number 255730231, within the International Research Training Group “Integrated engineering of continuous–discontinuous long fiber reinforced polymer structures” (GRK 2078). The support by the German Research Foundation (DFG) is gratefully acknowledged.

Appendix. Separating the first eigenvalue of the computed fiber orientation tensor of second order into two terms

The Appendix derives equation (3.17) for computing the shaking parameter $\Delta\varphi$. As starting point, we require that the first eigenvalue of the prescribed and the computed fiber orientation tensor of second order are equal:

$$a_1 \stackrel{!}{=} a_1^c. \quad (\text{A.1})$$

Using Eq. (3.12) leads to the equivalent formula

$$a_1 \stackrel{!}{=} \int_{-\infty}^{\infty} \int_{-\infty}^{\infty} \left[\tilde{a}_1^r p_1(\theta_1(\xi_\theta), \varphi_1(\xi_\varphi))^2 + \tilde{a}_2^r p_1(\theta_2(\xi_\theta), \varphi_2(\xi_\varphi))^2 \right] \psi(\xi_\theta) \psi(\xi_\varphi) d_\theta d_\varphi, \quad (\text{A.2})$$

where $p_1(\theta_i(\xi_\theta), \varphi_i(\xi_\varphi))$ denotes the first component of the fiber direction. We are interested in the influence of the shaking parameter $\Delta\varphi$ on the fiber orientation tensor of second order. Thus, we need an explicit formulation of the shaking procedure for the first component of the fiber direction. Following Eq. (2.1) the component is computed as

$$p_1(\theta_i(\xi_\theta), \varphi_i(\xi_\varphi)) = \sin(\theta_i(\xi_\theta)) \cos(\varphi_i(\xi_\varphi)). \quad (\text{A.3})$$

To proceed, we account for the sampling procedure of the angles (3.9) and are led to the expression

$$p_1(\theta_i(\xi_\theta), \varphi_i(\xi_\varphi)) = \sin(\tilde{\theta}_i + \Delta\theta \xi_\theta) \cos(\tilde{\varphi}_i + \Delta\varphi \xi_\varphi). \quad (\text{A.4})$$

With the initial angles (3.10), we obtain the explicit shaking procedure for the x -component of the fiber direction for both initial directions

$$\begin{aligned} p_1(\theta_1(\xi_\theta), \varphi_1(\xi_\varphi)) &= \sin\left(\frac{\pi}{2} + \Delta\theta \xi_\theta\right) \cos(\Delta\varphi \xi_\varphi) \\ p_1(\theta_2(\xi_\theta), \varphi_2(\xi_\varphi)) &= \sin\left(\frac{\pi}{2} + \Delta\theta \xi_\theta\right) \cos\left(\frac{\pi}{2} + \Delta\varphi \xi_\varphi\right). \end{aligned} \quad (\text{A.5})$$

To shorten the expressions (A.5), we use the reduction formulas for trigonometrical functions:

$$\begin{aligned} p_1(\theta_1(\xi_\theta), \varphi_1(\xi_\varphi)) &= \cos(\Delta\theta \xi_\theta) \cos(\Delta\varphi \xi_\varphi) \\ p_1(\theta_2(\xi_\theta), \varphi_2(\xi_\varphi)) &= -\cos(\Delta\theta \xi_\theta) \sin(\Delta\varphi \xi_\varphi). \end{aligned} \quad (\text{A.6})$$

With this insight at hand, we reformulate equation (A.2)

$$\begin{aligned} a_1 &\stackrel{!}{=} \int_{-\infty}^{\infty} \int_{-\infty}^{\infty} \left[\tilde{a}_1^r \cos(\Delta\theta \xi_\theta)^2 \cos(\Delta\varphi \xi_\varphi)^2 \right. \\ &\quad \left. + \tilde{a}_2^r \cos(\Delta\theta \xi_\theta)^2 \sin(\Delta\varphi \xi_\varphi)^2 \right] \psi(\xi_\theta) \psi(\xi_\varphi) d_\theta d_\varphi \\ &= \int_{-\infty}^{\infty} \int_{-\infty}^{\infty} \cos(\Delta\theta \xi_\theta)^2 \left[\tilde{a}_1^r \cos(\Delta\varphi \xi_\varphi)^2 \right. \\ &\quad \left. + \tilde{a}_2^r \sin(\Delta\varphi \xi_\varphi)^2 \right] \psi(\xi_\theta) \psi(\xi_\varphi) d_\theta d_\varphi \end{aligned} \quad (\text{A.7})$$

and uncover that the shaking parameters $\Delta\theta$ and $\Delta\varphi$ are considered in two decoupled terms. Hence, the double integral may be separated into

$$\begin{aligned} a_1 &\stackrel{!}{=} \int_{-\infty}^{\infty} \cos(\Delta\theta \xi_\theta)^2 \psi(\xi_\theta) d_\theta \int_{-\infty}^{\infty} \left[\tilde{a}_1^r \cos(\Delta\varphi \xi_\varphi)^2 \right. \\ &\quad \left. + \tilde{a}_2^r \sin(\Delta\varphi \xi_\varphi)^2 \right] \psi(\xi_\varphi) d_\varphi. \end{aligned} \quad (\text{A.8})$$

Let us recall equation (3.14), then we may reformulate the first integral of Eq. (A.8)

$$a_1 \stackrel{!}{=} (1 - a_3) \int_{-\infty}^{\infty} \left[\tilde{a}_1^r \cos(\Delta\varphi \xi_\varphi)^2 + \tilde{a}_2^r \sin(\Delta\varphi \xi_\varphi)^2 \right] \psi(\xi_\varphi) d_\varphi, \quad (\text{A.9})$$

leading to Eq. (3.17).

References

- [1] de Paiva RF, Bisiaux M, Lynch J, Rosenberg E. High resolution x-ray tomography in an electron microprobe. *Rev Sci Instrum* 1996;67(6):2251–6.
- [2] Shen H, Nutt S, Hull D. Direct observation and measurement of fiber architecture in short fiber-polymer composite foam through micro-CT imaging. *Compos Sci Technol* 2004;64(13–14):2113–20.
- [3] Matouš K, Geers MGD, Kouznetsova VG, Gillman A. A review of predictive nonlinear theories for multiscale modeling of heterogeneous materials. *J Comput Phys* 2017;330:192–220.
- [4] Kozlov SM. Averaging of differential operators with almost periodic rapidly oscillating coefficients. *Math USSR-Sbornik* 1978;107(149):199–217, (2 (10)).
- [5] Papanicolaou GC, Varadhan SRS. Boundary value problems with rapidly oscillating random coefficients. In: *Random fields, vol. I, II (Esztergom, 1979)*. *Colloq. Math. Soc. János Bolyai, vol. 27*, North-Holland, Amsterdam-New York; 1981, p. 835–73.
- [6] Kanit T, Forest S, Galliet I, Mounoury V, Jeulin D. Determination of the size of the representative volume element for random composites: statistical and numerical approach. *Int J Solids Struct* 2003;40(13–14):3647–79.
- [7] Schneider M, Josien M, Otto F. Representative volume elements for matrix-inclusion composites - a computational study on the effects of an improper treatment of particles intersecting the boundary and the benefits of periodizing the ensemble. *J Mech Phys Solids* 2022;158:104652.
- [8] Gitman IM, Askes H, Sluys LJ. Representative volume: Existence and size determination. *Eng Fract Mech* 2007;74(16):2518–34.
- [9] Salmi M, Auslender F, Bornert M, Fogli M. Apparent and effective mechanical properties of linear matrix-inclusion random composites: Improved bounds for the effective behavior. *Int J Solids Struct* 2012;49(10):1195–211.

- [10] Terada K, Hori M, Kyoya T, Kikuchi N. Simulation of the multi-scale convergence in computational homogenization approaches. *Int J Solids Struct* 2000;37(16):2285–311.
- [11] Trovalusci P, Bellis MLD, Ostoja-Starzewski M, Murrall A. Particulate random composites homogenized as micropolar materials. *Meccanica* 2014;49(11):2719–27.
- [12] Trovalusci P, Ostoja-Starzewski M, Bellis MLD, Murrall A. Scale-dependent homogenization of random composites as micropolar continua. *Eur J Mech A Solids* 2015;49:396–407.
- [13] Sab K, Nedjar B. Periodization of random media and representative volume element size for linear composites. *C R Mecanique* 2005;333(2):187–95.
- [14] Widom B. Random sequential addition of hard spheres to a volume. *J Chem Phys* 1966;44(10):3888–94.
- [15] Feder J. Random sequential adsorption. *J Theoret Biol* 1980;87(2):237–54.
- [16] Evans KE, Gibson AG. Prediction of the maximum packing fraction achievable in randomly oriented short-fibre composites. *Compos Sci Technol* 1986;25:149–62.
- [17] Toll S. Packing mechanics of fiber reinforcements. *Polym Eng. Sci.* 1998;38(8):1337–50.
- [18] Yang L, Yan Y, Ran Z, Liu Y. A new method for generating random fibre distributions for fibre reinforced composites. *Compos Sci Technol* 2013;76:14–20.
- [19] Tian W, Qi L, Zhou J, Ma Y. Representative volume element for composites reinforced by spatially randomly distributed discontinuous fibers and its applications. *Compos Struct* 2013;131(7):366–73.
- [20] Tian W, Chao X, Fu MW, Qi L. An advanced method for efficiently generating composite RVEs with specified particle orientation. *Compos Sci Technol* 2021;205:108647.
- [21] Chen L, Gu B, Zhou J, Tao J. Study of the effectiveness of the RVEs for random short fiber reinforced elastomer composites. *Fibers Polym* 2019;20(7):1467–79.
- [22] Bahmani A, Li G, Willett T, Montesano J. Three-dimensional micromechanical assessment of biomimetic composites with non-uniformly dispersed inclusions. *Compos Struct* 2019;212:484–99.
- [23] Advani SG, Tucker III CL. A numerical simulation of short fiber orientation in compression molding. *Polym Compos* 1990;11(3):164–73.
- [24] Görthofer J, Meyer N, Pallicy TD, Schöttl L, Trauth A, Schemmann M, et al. Virtual process chain of sheet molding compound: development, validation and perspectives. *Composites B* 2019;169:133–47.
- [25] Dray D, Gilormini P, Régnier G. Comparison of several closure approximations for evaluating the thermoelastic properties of an injection molded short-fiber composite. *Compos Sci Technol* 2007;67(7–8):1601–10.
- [26] Bernasconi A, Cosmi F, Hine PJ. Analysis of fibre orientation distribution in short fibre reinforced polymers: A comparison between optical and tomographic methods. *Compos Sci Technol* 2012;72(16):2002–8.
- [27] Li Z, Liu Z, Xue Y, Zhu P. A novel algorithm for significantly increasing the fiber volume fraction in the reconstruction model with large fiber aspect ratio. *J Ind Text* 2022;51(1):506–30.
- [28] Williams S, Philipse A. Random packings of spheres and spherocylinders simulated by mechanical contraction. *Phys Rev E* 2003;67(5):1–9.
- [29] Schneider M. The sequential addition and migration method to generate representative volume elements for the homogenization of short fiber reinforced plastics. *Comput Mech* 2017;59:247–63.
- [30] Schneider M. An algorithm for generating microstructures of fiber-reinforced composites with long fibers. *Internat J Numer Methods Engrg* 2022;Online:1–23.
- [31] Mehta A, Schneider M. A sequential addition and migration method for generating microstructures of short fibers with prescribed length distribution. *Comput Mech* 2022;70(4):829–51.
- [32] Müller V, Böhlke T. Prediction of effective elastic properties of fiber reinforced composites using fiber orientation tensors. *Compos Sci Technol* 2016;130:36–45.
- [33] Weibull W. A statistical distribution function of wide applicability. *J Appl Mech* 1951;18(3):293–7.
- [34] Bernasconi A, Cosmi F, Dreossi D. Local anisotropy analysis of injection moulded fibre reinforced polymer composites. *Compos Sci Technol* 2008;68:2574–81.
- [35] Hessman PA, Welschinger F, Hornberger K, Böhlke T. On mean field homogenization schemes for short fiber reinforced composites: Unified formulation, application and benchmark. *Int J Solids Struct* 2021;230–231:111141.
- [36] Fu SY, Yue CY, Hu X, Mai YW. Effects of fiber length and orientation distributions on the mechanical properties of short-fiber-reinforced polymers. A review. *Mater Sci Res Int* 1999;5(2):74–83.
- [37] Advani SG, Tucker III CL. The use of tensors to describe and predict fiber orientation in short fiber composites. *J Rheol* 1987;31:751–84.
- [38] Kanatani K-I. Distribution of directional data and fabric tensors. *Internat J Engrg Sci* 1984;22(2):149–64.
- [39] Hessman PA, Riedel T, Welschinger F, Hornberger K, Böhlke T. Microstructural analysis of short glass fiber reinforced thermoplastics based on x-ray micro-computed tomography. *Compos Sci Technol* 2019;183:107752.
- [40] Krause M, Hausherr JM, Burgeth B, Herrmann C, Krenkel W. Determination of the fibre orientation in composites using the structure tensor and local X-ray transform. *J Mater Sci* 2010;45(4):888–96.
- [41] Wirjadi O, Schladitz K, Easwaran P, Ohser J. Estimating fibre direction distributions of reinforced composites from tomographic images. *Image Anal Stereol* 2016;35(3):167–79.
- [42] Bauer JK, Böhlke T. On the dependence of orientation averaging mean field homogenization on planar fourth-order fiber orientation tensors. *Mech Mater* 2022;170:104307.
- [43] Papoulis AP, Unnikrishna Pillai S. Probability, random variables, and stochastic processes. 4th ed.. Boston: McGraw-Hill; 2002.
- [44] Hammersley JM, Handscomb DC. Monte Carlo methods. London: Chapman and Hall; 1964.
- [45] Sobol IM. On the distribution of points in a cube and the approximate evaluation of integrals. *USSR Comput Math Math Phys* 1967;7(4):86–112.
- [46] Sobol IM. Uniformly distributed sequences with additional uniformity properties. *USSR Comput Math Math Phys* 1967;16(5):236–42.
- [47] Pan Y, Pelegri AA, Iorga L. Analysis of 3D random chopped fiber reinforced composite using the finite element method. *Comput Mater Sci* 2008;43(3):450–61.
- [48] Böhm HJ, Eckschlagner A, Han W. Multi-inclusion unit cell models for metal matrix composites with randomly oriented discontinuous reinforcements. *Comput Mater Sci* 2002;25(1–2):42–53.
- [49] Vega C, Lago S. A fast algorithm to evaluate the shortest distance between rods. *Comput Chem* 1994;67–68:56–70.
- [50] Pournin I, Weber M, Tsukahara M, Ferrez JA, Ramaoli M, Liebling TM. Three-dimensional distinct element simulation of spherocylinder crystallization. *Granul Matter* 2005;7:119–26.
- [51] Deiters UK. Efficient coding of the minimum image convention. *Z Phys Chem* 2013;227(2–3):345–52.
- [52] Naghipour P, Bartsch M, Chernova L, Hausmann J, Voggenreiter H. Effect of fiber angle orientation and stacking sequence on mixed mode fracture toughness of carbon fiber reinforced plastics: numerical and experimental investigations. *Mater Sci Eng A* 2010;527(3):509–17.
- [53] Breuer K, Stommel M. RVE modelling of short fiber reinforced thermoplastics with discrete fiber orientation and fiber length distribution. *SN Appl Sci* 2019;2:91.
- [54] Moulinec H, Suquet P. A fast numerical method for computing the linear and nonlinear mechanical properties of composites. *C R Acad Sci Ser II* 1994;318(11):1417–23.
- [55] Moulinec H, Suquet P. A numerical method for computing the overall response of nonlinear composites with complex microstructure. *Comput Methods Appl Mech Eng* 1998;157:69–94.
- [56] Schneider M, Ospald F, Kabel M. Computational homogenization of elasticity in a staggered grid. *Internat J Numer Methods Engrg* 2016;105(9):693–720.
- [57] Zeman J, Vondřejc J, Novák J, Marek I. Accelerating a FFT-based solver for numerical homogenization of periodic media by conjugate gradients. *J Comput Phys* 2010;229(21):8065–71.
- [58] Brisard S, Dormieux L. Combining Galerkin approximation techniques with the principle of hashin and shtrikman to derive a new FFT-based numerical method for the homogenization of composites. *Comput Methods Appl Mech Engrg* 2012;217–220:197–212.
- [59] Schneider M. A review of non-linear FFT-based computational homogenization methods. *Acta Mech* 2021;232:2051–100.
- [60] Görthofer J, Schneider M, Ospald F, Hrymak A, Böhlke T. Computational homogenization of sheet molding compound composites based on high fidelity representative volume elements. *Comput Mater Sci* 2020;174:109456.
- [61] Cowin SC. The relationship between the elasticity tensor and the fabric tensor. *Mech Mater* 1985;4(2):137–47.
- [62] Duschlbauer D, Böhm HJ, Pettermann HE. Computational simulation of composites reinforced by planar random fibers: Homogenization and localization by unit cell and mean field approaches. *J Compos Mater* 2006;40(24):2217–34.
- [63] Iorga L, Pan Y, Pelegri A. Numerical characterization of material elastic properties for random fiber composites. *Mech Mater Struct* 2008;3(7):1279–98.
- [64] Böhlke T, Brüggemann C. Graphical representation of the generalized Hooke's law. *Tech Mech* 2001;21(2):145–58.
- [65] Schneider M. Convergence of FFT-based homogenization for strongly heterogeneous media. *Math Methods Appl Sci* 2015;38(13):2761–78.
- [66] Müller V, Kabel M, Andrä H, Böhlke T. Homogenization of linear elastic properties of short-fiber reinforced composites – A comparison of mean field and voxel-based methods. *Int J Solids Struct* 2015;(67–68):56–70.
- [67] Hill R. Elastic properties of reinforced solids: Some theoretical principles. *J Mech Phys Solids* 1963;11(5):357–72.
- [68] Drugan WJ, Willis JR. A micromechanics-based nonlocal constitutive equations and estimates of representative volume element size for elastic composites. *J Mech Phys Solids* 1996;44:497–524.
- [69] Gloria A, Otto F. An optimal variance estimate in stochastic homogenization of discrete elliptic equations. *Ann Probab* 2011;39(3):779–856.
- [70] Dirrenberger J, Forest S, Jeulin D. Towards gigantic RVE sizes for 3D stochastic fibrous networks. *Int J Solids Struct* 2014;51(2):359–76.
- [71] Jeulin D. Power laws variance scaling of boolean random varieties. *Methodol Comput Appl Probab* 2016;18(4):1065–79.
- [72] Folgar F, Tucker III CL. Orientation behaviour of fibers in concentrated suspensions. *J Reinf Plast Compos* 1984;3:98–119.
- [73] Cintra JS, Tucker III CL. Orthotropic closure approximations for flow-induced fiber orientation. *J Rheol* 1995;39(6):1095–122.

- [74] Kugler SK, Kech A, Cruz C, Osswald T. Fiber orientation predictions - A review of existing models. *J Compos Sci* 2020;4(2):69.
- [75] Breuer K, Stommel M, Korte W. Analysis and evaluation of fiber orientation reconstruction methods. *J Compos Sci* 2019;3(3):67.
- [76] Bauer JK, Böhlke T. Variety of fiber orientation tensors. *Math Mech Solids* 2022;27(7):1185–211.
- [77] Montgomery-Smith S, He W, Jack D, Smith DE. Exact tensor closures for the three-dimensional Jeffery's equation. *J Fluid Mech* 2011;680:321–35.
- [78] Montgomery-Smith S, Jack D, Smith DE. The fast exact closure for Jeffery's equation with diffusion. *J Non-Newton Fluid Mech* 2011;166:343–53.
- [79] Chaubal CV, Leal L. A closure approximation for liquid-crystalline polymer models based on parametric density estimation. *J Rheol* 1998;42(1):177.
- [80] Bauer JK, Böhlke T. Fiber orientation distributions based on planar fiber orientation tensors of fourth order. *Math Mech Solids* 2022;Online:1–22.
- [81] Bay RS, Tucker III CL. Fiber orientation in simple injection moldings. Part I: Theory and numerical methods. *Polym Compos* 1992;13(4):317–31.
- [82] Bay RS, Tucker III CL. Fiber orientation in simple injection moldings. Part II: Experimental results. *Polym Compos* 1992;13(4):332–41.
- [83] Breuer K, Spickenheuer A, Stommel M. Statistical analysis of mechanical stressing in short fiber reinforced composites by means of statistical and representative volume elements. *Fibers* 2021;9(5):32.